


Cite this: *Mater. Adv.*, 2023,  
4, 3010

# 1D aligned, n–p and n–n type ZnO heterojunction nanofibers for NO<sub>2</sub> sensors: exploration of conduction mechanism using *in situ* impedance spectroscopy†

Ramakrishnan Vishnuraj, Mahaboobbatcha Aleem, Keerthi G Nair and  
Biji Pullithadathil \*

Highly aligned 1D n–p type ZnO/Bi<sub>2</sub>O<sub>3</sub> and n–n type ZnO/In<sub>2</sub>O<sub>3</sub> heterojunction nanofibers (HNFs) have been developed using coaxial electrospinning approach, aiming at exploring the effect of 1D aligned heterojunction nanofibrous structure on their NO<sub>2</sub> sensing properties. The aligned HNFs have been structurally and morphologically characterized using various spectroscopic and microscopic analyses. The n–p heterojunctions of ZnO/Bi<sub>2</sub>O<sub>3</sub> NFs and n–n heterojunctions of ZnO/In<sub>2</sub>O<sub>3</sub> NFs exhibited significantly boosted sensitivity towards NO<sub>2</sub> compared to pristine ZnO NFs. The superior responses of ZnO/Bi<sub>2</sub>O<sub>3</sub> and ZnO/In<sub>2</sub>O<sub>3</sub> HNFs have been attributed to their unique electron transport properties originated from work function differences, leading to the formation of interfacial accumulation and depletion of electrons resulting in surface band bending. The charge depletion of Bi<sub>2</sub>O<sub>3</sub>/ZnO HNFs was estimated to be higher due to the interaction of NO<sub>2</sub> gas at an operating temperature of 300 °C, resulting in quick response time (8–10 s) and 10 times superior sensitivity than ZnO NFs. Whereas, n–In<sub>2</sub>O<sub>3</sub>/n–ZnO HNFs-based sensor exhibited a reduced operating temperature (200 °C) with superior sensitivity ( $S \sim 340\%$ ), rapid response (5–7 s) with minimal interference towards exposure to trace-level NO<sub>2</sub> (500 ppb). The complex sensing mechanisms associated with n–p/n–n type HNFs have been deduced using *in situ* AC impedance spectroscopic studies, which endorsed the contributions from the modulation of grain and grain boundary resistance and charge transfer between n–p and n–n type materials. The results suggest that the boosted gas sensing properties of aligned 1D n–p and n–n type HNFs under atmospheric pressure conditions can pave the way for development of inexpensive and highly sensitive NO<sub>2</sub> gas sensors.

Received 25th December 2022,  
Accepted 4th June 2023

DOI: 10.1039/d2ma01095j

rsc.li/materials-advances

## 1. Introduction

Owing to the rapid expansion of automobiles and industries, environmental pollution arising from the emissions of hazardous nitrogen dioxide (NO<sub>2</sub>) causes severe ecological deprivation posing serious threats to human health.<sup>1,2</sup> Although various sensors based on metal oxide semiconductors (MOS) and composites have been deployed for sensing NO<sub>2</sub> for environmental monitoring applications, sensitivity and selectivity were found to be challenging, especially during trace level detection.<sup>3</sup> Among various MOSSs, ZnO-based gas sensors were extensively studied owing to the unique physicochemical properties.<sup>4–6</sup> Recently, various surface engineered strategies

for MOS-based heterojunction materials have been explored for imparting superior response and selectivity towards trace-level detection of NO<sub>2</sub>.<sup>7–10</sup> Pursuant to the nature of semiconductors, formation of n–p and n–n type modifications of MOS can be considered as an efficacy behind enhanced NO<sub>2</sub> sensor performance.<sup>11,12</sup> Typically, MOS heterojunctions are electrically connected through Fermi level ( $E_F$ ) alignment, *i.e.*, electrons transfer from higher energy state to the lower energy state until the Fermi level achieves equilibrium, which develops a depletion layer at the interface.<sup>13</sup> Eventually, potential barriers will be formed across the interface due to band bending.<sup>14</sup> Consequently, electrons accumulate at one interface in n–p and n–n heterojunctions leading to an increase in the electron density in the systems.<sup>15,16</sup> However, the charge carriers get depleted at the opposite side of the heterojunction interface, which could overcome the potential barrier and further transfer the electrons to interacting gas molecules. Among various types of heterojunction materials, dual MOS type heterojunction interfaces are most suitable for detailed understanding about

Nanosensor Laboratory, Department of Chemistry & Nanoscience and Technology,  
PSG Institute of Advanced Studies, Coimbatore–641 004, India.  
E-mail: [bijuja123@yahoo.co.in](mailto:bijuja123@yahoo.co.in), [pbm@psgias.ac.in](mailto:pbm@psgias.ac.in)

† Electronic supplementary information (ESI) available. See DOI: <https://doi.org/10.1039/d2ma01095j>



NO<sub>2</sub> detection mechanisms. Although many reports in the literature have attempted to explore the significance of n-p and n-n type structural modifications towards enhancement in NO<sub>2</sub> sensor response and selectivity under reduced operating temperature, a concrete understanding of complex sensing mechanism focusing on quantitative contributions of p- and n-type heterojunctions on MOS is not yet available.

Among various morphologies, one-dimensional (1D) heterojunction nanostructures have exhibited desirable properties such as high aspect ratio and large surface area leading to elevated gas-sensing properties, which have been found to be more suitable for device integration.<sup>17–22</sup> Moreover, in the case of 1D heterojunction MOS materials, the radial modulation of the hole-accumulation layer (HAL) is intensified for shell materials thinner than the Debye length.<sup>23</sup> In contrast, the contribution of volume fraction to resistance modulation is found to be weakened. Therefore, modulation of heterojunction morphological arrangement has to be seriously considered when designing a heterojunction MOS-based sensing material, since the NO<sub>2</sub> adsorption process fully depends on the surface anchored p- or n-type heterojunctions. Recently, Kim *et al.* explored the significance of expansion of the HAL in n-p type SnO<sub>2</sub>-Cu<sub>2</sub>O core-shell nanowire during NO<sub>2</sub> sensing performances.<sup>24</sup> It was revealed that the NO<sub>2</sub> response deteriorated for SnO<sub>2</sub>-Cu<sub>2</sub>O owing to the existence of a thicker Cu<sub>2</sub>O shell layer, while an increase in the p-layer is restricted by the presence of p-n interface, which act as a blocking layer at the SnO<sub>2</sub> sites. In the case of n-n heterojunction materials, Sun *et al.* explored the NO<sub>2</sub> gas sensing characteristics of n-CaO/n-ZnO nanorods, which showed improved sensing performance.<sup>25</sup> This is mostly due to the higher variation in barrier potential near the n-CaO/n-ZnO heterojunction during exposure to NO<sub>2</sub>.

In general, the chemiresistive gas sensing mechanism is purely based on the variations in electrical resistance of a MOS upon gas exposure, which is induced by gas-solid interactions.<sup>26,27</sup> The formation of potential barrier energy at the inter-particle interfaces could have the nature of Schottky conduction. However, the conduction mechanism in n-p and n-n type MOS heterojunction materials during charge transfer is still unclear and also a comprehensive understanding of the Schottky barrier formation mechanism in such hybrid materials is crucial for development of superior gas sensor devices. Various *in situ* techniques have been used to investigate the gas sensing mechanism mediated by charge transfer process, intrinsic defects *etc.* in various heterojunction nanostructures.<sup>28–35</sup> *In situ* alternating current (AC) impedance spectroscopy is a promising and most sensitive technique, which is capable of characterizing the physicochemical processes and of revealing the conduction mechanisms in heterojunction MOSs during gas exposure.<sup>36</sup> Generally, direct current (DC) measurements can provide information on device performance such as sensitivity, selectivity and response time. Whereas, AC-based impedance measurements help to categorize and quantify the specific properties responsible for enhanced sensor performances like bulk grain properties, grain boundary properties and interfacial properties of transducers and active sensing regions.<sup>37</sup> Impedance spectroscopy can

also be used to estimate the donor concentration and depletion region width, in addition to the relative contributions of interfacial and bulk mechanisms towards total conductivity of materials as a function of the working temperature and gas atmosphere.<sup>38</sup> Recently, Maziarz *et al.* investigated the effect of n-n (SnO<sub>2</sub>-TiO<sub>2</sub>) and p-n (CuO-TiO<sub>2</sub>) heterostructured nanolayers on NO<sub>2</sub> detection.<sup>11</sup> Based on impedance analysis, improved NO<sub>2</sub> detection characteristics of the n-SnO<sub>2</sub>/n-TiO<sub>2</sub> heterostructures was attributed to formation of heterointerfaces and larger surface-to-volume ratio. Nevertheless, n-TiO<sub>2</sub>/p-CuO heterostructures exhibited reduced NO<sub>2</sub> responses, which might be ascribed to the effect of charge compensation. Also, Wang *et al.* performed *in situ* AC impedance analysis for NiO-WO<sub>3</sub> nanorods before and after H<sub>2</sub>S exposure and revealed that the grain-grain boundary interaction along with p-n junction contributing effect could be the reason behind the superior sensing performance.<sup>39</sup> So far, a quantitative approach to unveil the complex sensing phenomenon associated with heterojunction materials during NO<sub>2</sub> exposure has not yet been reported.

In this investigation, an on-chip fabrication strategy for creating 1D aligned n-p ZnO/Bi<sub>2</sub>O<sub>3</sub> and n-n ZnO/In<sub>2</sub>O<sub>3</sub> HNFs has been developed based on coaxial electrospinning for NO<sub>2</sub> gas sensor applications. The effect of n-p and n-n contributions and nano-grain-grain boundary interactions of the materials during NO<sub>2</sub> exposure was investigated by *in situ* AC impedance spectroscopic studies. This study can contribute significantly towards selection of appropriate surface engineering approaches and process conditions for fabrication of high-performance low-cost aligned heterojunction nanowire sensor devices.

## 2. Experimental section

### Materials

Zinc acetate (98%, Merck), bismuth nitrate pentahydrate (99.8%, Merck), indium chloride (99.7%, Sigma-Aldrich), polyvinyl alcohol (MW: 130 000, Sigma-Aldrich), polyvinyl pyrrolidone (MW: 200 000, Sigma-Aldrich), copper foil, ethanol (Merck) and *N,N*-dimethylformamide (DMF; Merck) were used without any further purification. Deionized (Type-I) water was used for all synthesis. All the reagents involved in the experiments were of analytical grade and were directly used without further purification.

### Method

An in-house electrospinning unit with independently controlled dual syringe pump (HOLMARC) was used to synthesize MOS HNFs using coaxial electrospinning. A DC power supply of 30 kV (Glassman) was utilized in this system. A Teflon-based coaxial spinneret was used for coaxial electrospinning of the materials. 1D aligned coaxial type n-ZnO/p-Bi<sub>2</sub>O<sub>3</sub> and n-ZnO/n-In<sub>2</sub>O<sub>3</sub> HNFs were developed using a coaxial electrospinning process. The in-house built coaxial electrospinning set-up was equipped with independently controlled dual syringe pump for feed fluid supply, coaxial spinneret assembly with concentric nozzles and parallel type copper collector plate.



In this typical process, feed solution A was prepared by dissolving 1.2 g zinc acetate in 8 wt% of PVA (polyvinyl alcohol) dissolved in a binary solution containing 10 mL deionized water and 2.5 mL ethanol. After continuous stirring at 60 °C for 3 h, a homogeneous feed solution A was obtained. For preparing feed solution B, 0.2 wt% Bi(NO<sub>3</sub>)<sub>3</sub> solution and 10 wt% of PVP (polyvinyl pyrrolidone) dissolved in 10 mL DMF were mixed to obtain a viscous solution. The pale white solution was immediately stirred for 2 h. Feed solution C was prepared by stirring a mixture of 0.5 wt% InCl<sub>2</sub> solution and 12 wt% of PVP in 10 mL DMF for 4 h to obtain a viscous solution.

### 2.1. Synthesis of 1D aligned n-ZnO/p-Bi<sub>2</sub>O<sub>3</sub> HNFs

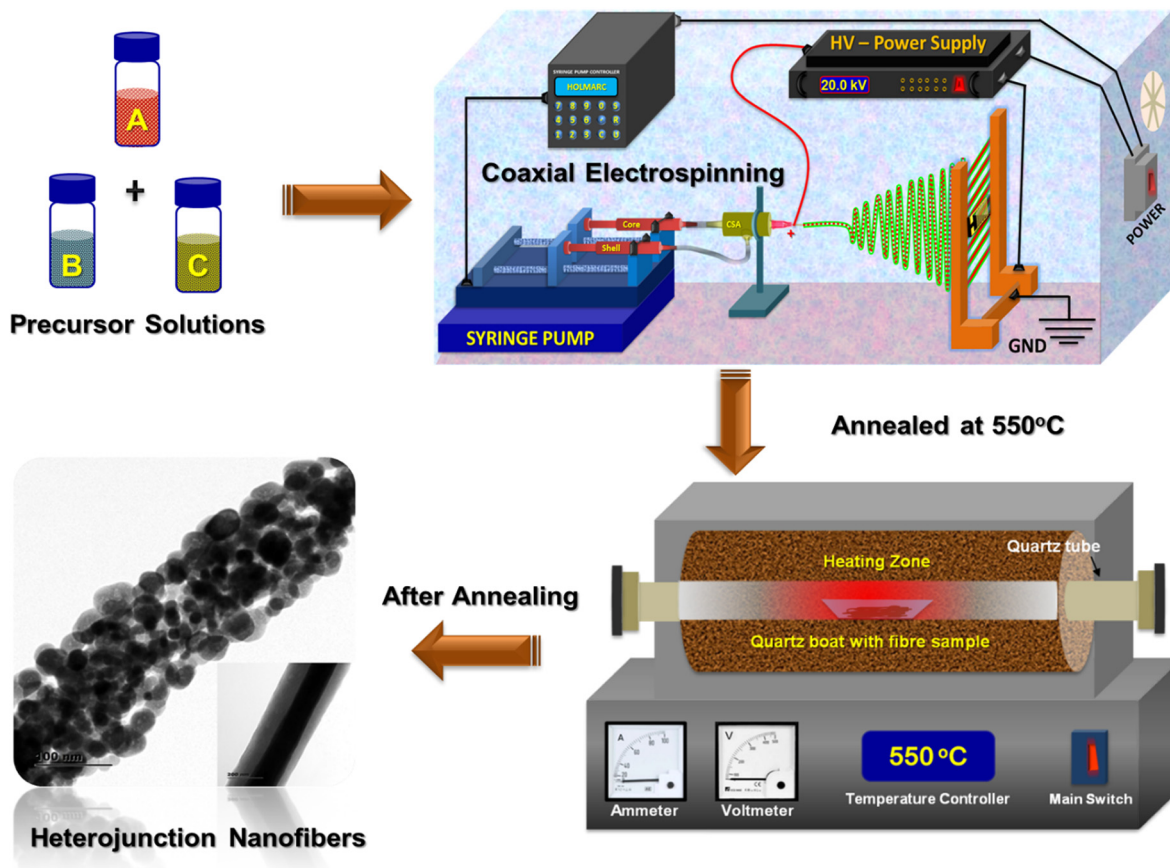
1D aligned n-ZnO/p-Bi<sub>2</sub>O<sub>3</sub> HNFs were fabricated by coaxial electrospinning method. The inner fluid (solution A) was taken as core liquid and the outer shell was taken as solution B. The prepared precursor solution was then transferred into plastic syringes for electrospinning. The precursors were coaxially electrospun from a stainless-steel needle (21 gauge for inner fluid and 18G for outer fluid) attached to the coaxial spinneret assembly. Specifically, the feed rates of inner-core and outer-shell solutions were fixed as 0.4 mL h<sup>-1</sup> and 1 mL h<sup>-1</sup>, respectively, which were controlled using a dual syringe pump. DC voltage of 18 kV was supplied between the needle and collector which was kept at a distance of 21 cm for electrospinning.

### 2.2. Synthesis of 1D aligned n-ZnO/n-In<sub>2</sub>O<sub>3</sub> HNFs

As shown in Scheme 1, the n-ZnO/n-In<sub>2</sub>O<sub>3</sub> NFs were fabricated by the coaxial electrospinning method. Solution A and solution C were taken as the inner-core and outer-shell fluids respectively. The precursors were coaxially electrospun using stainless-steel needles (22G for inner fluid and 19G for outer fluid) attached to the coaxial spinneret assembly. The fluid speeds of inner-core and outer-shell solutions were fixed as 0.8 mL h<sup>-1</sup> and 1 mL h<sup>-1</sup> respectively, which were further controlled using a dual syringe pump. In this experiment, a 20 kV DC voltage was applied to the needle and the collector (separated with a distance of 18 cm) for electrospinning. As-electrospun core-shell samples of Zn(CH<sub>3</sub>COO)<sub>2</sub>/PVA/core-PVP/Bi(NO<sub>3</sub>)<sub>3</sub> shell and Zn(CH<sub>3</sub>COO)<sub>2</sub>/PVA/core-PVP/InCl<sub>2</sub> shell composites were further calcined at 550 °C for 3 h under oxygen environment using a tubular controlled atmosphere furnace with a heating rate of 5 °C min<sup>-1</sup> to obtain crystalline n-ZnO/p-Bi<sub>2</sub>O<sub>3</sub> and n-ZnO/n-In<sub>2</sub>O<sub>3</sub> HNFs.

### 2.3. In situ AC impedance spectroscopic studies

*In situ* AC impedimetric studies were performed in order to explore the grain-grain boundary mediated conduction mechanism of 1D n-ZnO/p-Bi<sub>2</sub>O<sub>3</sub> and n-ZnO/n-In<sub>2</sub>O<sub>3</sub> HNFs under air and NO<sub>2</sub> atmospheres. The heterojunction sensor was installed on the heating stage inside a custom-made gas sensor test station in our laboratory, which is connected with a Eurotherm



Scheme 1 Schematic illustration of coaxial electrospinning of aligned ZnO/Bi<sub>2</sub>O<sub>3</sub> and ZnO/In<sub>2</sub>O<sub>3</sub> HNFs.



temperature controller. The impedance spectra were acquired using a CHI600E electrochemical workstation (CH Instruments, Inc., USA). A constant 100 sccm of  $\text{NO}_2$  was purged under dynamic state with nitrogen as carrier. An initial voltage of 0.5 V with an amplitude of 0.06 V and frequency range up to 10 MHz was used for all the experiments in order to acquire Nyquist plots.

### 3. Results and discussion

Highly aligned 1D n-ZnO/p- $\text{Bi}_2\text{O}_3$  and n-ZnO/n- $\text{In}_2\text{O}_3$  heterostructured nanofibers were directly spun onto IDA microelectrodes using the coaxial electrospinning method (Fig. S1(a and b), ESI<sup>†</sup>) and later annealed at 550 °C as depicted in Scheme 1. The heterostructured NFs were aligned transversely on the IDA fingers following the field of electric lines as evidenced by simulations as reported in our previous work.<sup>40</sup> During thermal oxidation, polymeric template was decomposed with formation of p-type  $\text{Bi}_2\text{O}_3$  and n-type  $\text{In}_2\text{O}_3$  nanoislands anchored on wurtzite ZnO nanofibers forming n-p and n-n type heterojunction interfaces, respectively, which were obtained as porous nanofibers. Fig. S1(d and e) (ESI<sup>†</sup>) presents electron microscopic images of 1D aligned ZnO-based HNFs deposited on an IDA chip before the annealing process. The as-obtained NFs were observed to be highly aligned and of more than a few micrometers in length which are suitable for electronics and sensor applications. Further, from AFM topographic data depicted in Fig. S1(f) (ESI<sup>†</sup>), HNFs possessed a 1D nanograined structure after annealing.

#### 3.1. Structural analysis of $\text{ZnO}/\text{Bi}_2\text{O}_3$ and $\text{ZnO}/\text{In}_2\text{O}_3$ HNFs

The crystal structures of pristine ZnO,  $\text{ZnO}/\text{Bi}_2\text{O}_3$  and  $\text{ZnO}/\text{In}_2\text{O}_3$  HNFs were studied using powder XRD as depicted in Fig. 1(a). Highly intense peaks appeared at  $2\theta$  values of 31.697°, 34.325°, 36.357°, 47.416°, 56.507°, 62.769°, 67.867° and 69.6° corresponding to the hexagonal wurtzite structure of ZnO along the crystal planes of (100), (002), (101), (102), (110), (103), (112), and (201), respectively, which are well matched with JCPDS PDF no. 36-1451 for pristine ZnO nanofibers.<sup>41</sup> Fig. 1(a) depicts the diffraction peaks of n-ZnO/p- $\text{Bi}_2\text{O}_3$  NFs, signifying the existence of heterojunctions and structural purity of the NFs. The coexistence of the peaks indicates the formation of  $\text{Bi}_2\text{O}_3$  nanoislands (NIs) along with characteristic ZnO peaks such as (002), (102), (202), (130), (221) and (321) which confirmed that the  $\text{Bi}_2\text{O}_3$  NIs exhibited  $\alpha$ - $\text{Bi}_2\text{O}_3$  monoclinic structure as inferred from JCPDS no. 71-0465. No further peaks or peak shift were detected in the case of porous, nanograined n-ZnO/p- $\text{Bi}_2\text{O}_3$  NFs confirming the anchoring of p- $\text{Bi}_2\text{O}_3$  NIs onto the ZnO NFs.<sup>42</sup> Whereas, in the case of n-ZnO/n- $\text{In}_2\text{O}_3$  HNFs, along with wurtzite ZnO lattice planes, the occurrence of (012), (104), (110), (332), (431) (440), (541) and (217) lattice planes confirmed the formation of heterointerface of  $\text{In}_2\text{O}_3$  NIs with rhombohedral structure as inferred from JCPDS no. 73-1809. It is also evident from Fig. 1(a) that no peak shift was observed and thereby no interstitial doping of  $\text{In}_2\text{O}_3$  in ZnO occurred while forming nanofibers by coaxial spinning approach while forming the core-shell structure.<sup>43</sup>

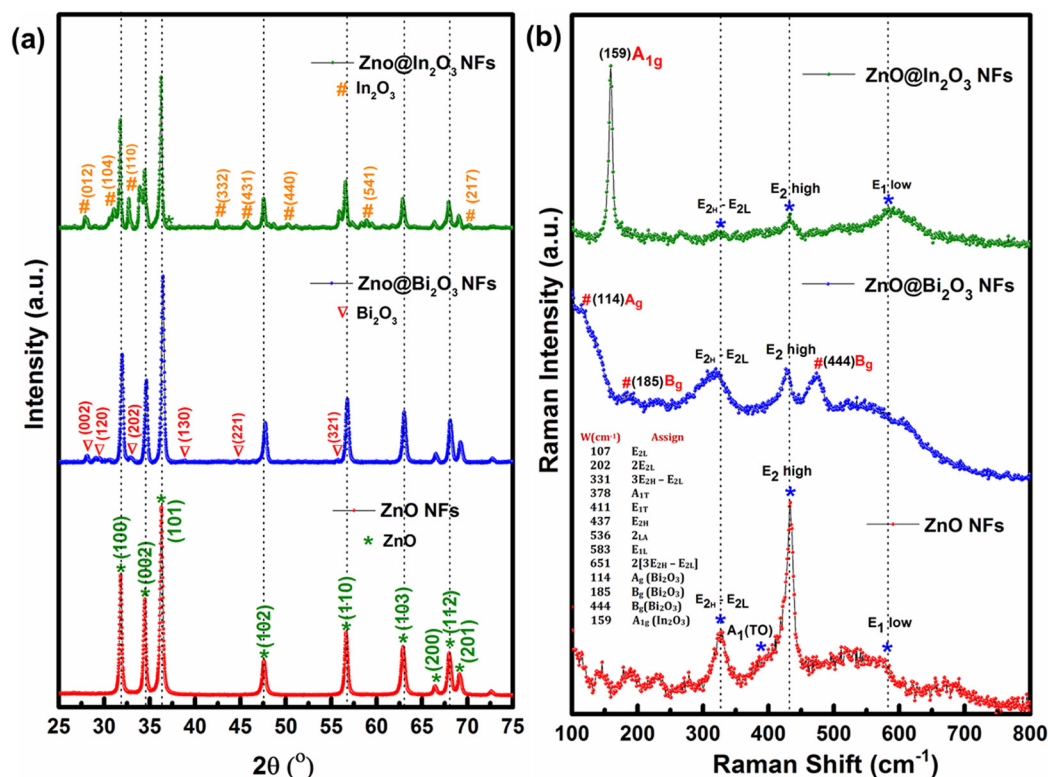


Fig. 1 (a) XRD patterns and (b) Raman spectra of pristine ZnO,  $\text{ZnO}/\text{Bi}_2\text{O}_3$  and  $\text{ZnO}/\text{In}_2\text{O}_3$  HNFs.

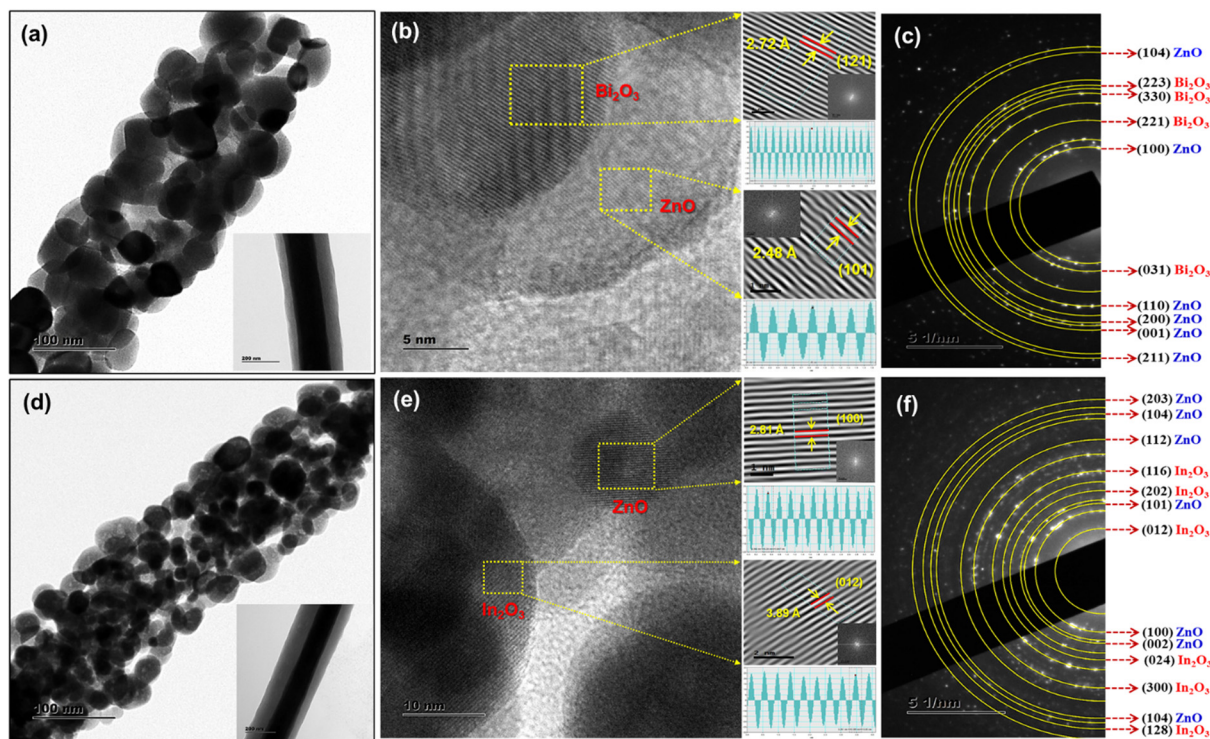


Fig. 1(b) depicts a comparison of Raman spectra acquired for pristine ZnO and n-ZnO/p-Bi<sub>2</sub>O<sub>3</sub> and n-ZnO/n-In<sub>2</sub>O<sub>3</sub> HNFs using the backscattering approach. Raman vibrational spectra of pure ZnO NFs were collected under ambient conditions which displayed a strong peak at 438 cm<sup>-1</sup> corresponding to E<sub>2high</sub> vibration of ZnO that confirms the hexagonal wurtzite crystal phase. The strong peak of E<sub>2</sub> mode confirmed the crystalline purity of ZnO NFs. The other two bands arise at the regions of lower wavenumber at 330 cm<sup>-1</sup> and 378 cm<sup>-1</sup> corresponding to the E<sub>2high</sub>-E<sub>2low</sub> and A<sub>1</sub>(TO) phonon vibrations modes. Similarly, the peaks observed at 330 cm<sup>-1</sup> and 437 cm<sup>-1</sup> can be ascribed to ZnO-zone boundary phonon vibrations.<sup>44</sup> However, the peaks arising for ZnO in ZnO/Bi<sub>2</sub>O<sub>3</sub> and ZnO/In<sub>2</sub>O<sub>3</sub> HNFs were found to exhibit considerable peak shifts as described in Fig. 1(b), because of the accommodation of p-Bi<sub>2</sub>O<sub>3</sub> and n-In<sub>2</sub>O<sub>3</sub> NIs on ZnO surface. For n-p type ZnO/Bi<sub>2</sub>O<sub>3</sub> HNFs, along with ZnO vibrations, the Raman shift observed at 114 cm<sup>-1</sup> is revealed as A<sub>g</sub> symmetry mode mainly due to the presence Bi atoms. The bands at 138 cm<sup>-1</sup> (A<sub>g</sub>), 185 cm<sup>-1</sup>, 444 cm<sup>-1</sup> (B<sub>g</sub>) might originate from the vibrations of both Bi<sup>3+</sup> and O<sup>2-</sup> ions onto ZnO further confirming the effective formation of heterojunction with monoclinic α-Bi<sub>2</sub>O<sub>3</sub> NIs. The E<sub>2</sub>(high) vibration peak in ZnO turns out to be quenched owing to the formation of p-Bi<sub>2</sub>O<sub>3</sub> heterojunction with n-ZnO. Also, oxygen vacancies (V<sub>o</sub>) and zinc interstitial (Zn<sub>in</sub>) states can be confirmed from the disappearance of A<sub>1</sub>(LO) peak.<sup>45</sup> Whereas, n-n type ZnO/In<sub>2</sub>O<sub>3</sub> HNFs exhibited a highly intense

peak at 159 cm<sup>-1</sup> as presented in Fig. 1(b) revealing the presence of n-In<sub>2</sub>O<sub>3</sub> NIs along with the significant n-ZnO bands. The intensity of all the peaks was quenched owing to the formation of n-In<sub>2</sub>O<sub>3</sub> NIs onto the n-ZnO NFs. The vibration band associated with E<sub>1-LO</sub> vibrations of n-ZnO was reduced because of the interstitial defects, which represents a promising region for the growth of n-In<sub>2</sub>O<sub>3</sub> NIs. Further, E<sub>2high</sub> vibrations were observed to be broad and weak, which confirms the heterojunction formation of In-O with Zn-O bonds.<sup>46</sup> A wide hump revealed at 584 cm<sup>-1</sup> ascribed to the E<sub>1-LO</sub> vibrations of n-ZnO confirms the existence of high-density oxygen vacancies (V<sub>o</sub>) and zinc interstitials (Zn<sub>i</sub>) in the materials. The formation of heterojunctions in the n-p and n-n type nanofibers promotes local electron transfer that can be revealed from the quenched vibrations of E<sub>2high</sub> and E<sub>1</sub>(LO) with substantial peak shifts found for both n-ZnO/p-Bi<sub>2</sub>O<sub>3</sub> and n-ZnO/n-In<sub>2</sub>O<sub>3</sub> HNFs that may enhance the NO<sub>2</sub> sensing characteristics.

### 3.2. Morphological characterization of ZnO/Bi<sub>2</sub>O<sub>3</sub> and ZnO/In<sub>2</sub>O<sub>3</sub> HNFs

To gain more insights into the nanograined structure and heterojunctions of the ZnO/Bi<sub>2</sub>O<sub>3</sub> and ZnO/In<sub>2</sub>O<sub>3</sub> nanofibers, TEM analysis was performed. Fig. 2 depicts TEM and high-resolution TEM images and the corresponding selective area electron diffraction (SAED) patterns of n-ZnO/p-Bi<sub>2</sub>O<sub>3</sub> and n-ZnO/n-In<sub>2</sub>O<sub>3</sub> HNFs. Fig. 2(a and d) displays low-magnification images of ZnO/Bi<sub>2</sub>O<sub>3</sub> and ZnO/In<sub>2</sub>O<sub>3</sub> HNFs, confirming the



**Fig. 2** (a) TEM images of n-ZnO/p-Bi<sub>2</sub>O<sub>3</sub> HNFs (inset shows the as-spun core-shell nanofiber). (b) HRTEM image of n-ZnO/p-Bi<sub>2</sub>O<sub>3</sub> HNFs and inverse FFT images of ZnO and Bi<sub>2</sub>O<sub>3</sub> (inset shows the live FFT images of ZnO and Bi<sub>2</sub>O<sub>3</sub>). (c) SAED pattern of n-ZnO/p-Bi<sub>2</sub>O<sub>3</sub> HNFs. (d) TEM images of n-ZnO/n-In<sub>2</sub>O<sub>3</sub> HNFs (inset shows the as-spun core-shell nanofiber). (e) HRTEM image of n-ZnO/n-In<sub>2</sub>O<sub>3</sub> NFs and inverse FFT images of ZnO and In<sub>2</sub>O<sub>3</sub> (inset shows the live FFT images of ZnO and In<sub>2</sub>O<sub>3</sub>). (f) SAED pattern of n-ZnO/n-In<sub>2</sub>O<sub>3</sub> HNFs.



nanograined morphology with high porosity, which can enhance the surface area and more active sites favouring the adsorption of target NO<sub>2</sub> gas. The inset shows the TEM image of as-spun single nanofiber where the contrast clearly depicts the core-shell structure that can further limit the lattice doping during the annealing process which plays a crucial role in forming an effective heterojunction. From Fig. 2(a and d), the average grain sizes were estimated as 36 ± 6 nm for n-ZnO/p-Bi<sub>2</sub>O<sub>3</sub> and 28 ± 4 for n-ZnO/n-In<sub>2</sub>O<sub>3</sub> HNFs and having lengths of several micrometers with high aspect ratio, suitable for electronics and sensing applications. Fig. 2(b and e) presents the HRTEM images of n-ZnO/p-Bi<sub>2</sub>O<sub>3</sub> and ZnO/In<sub>2</sub>O<sub>3</sub> HNFs, which clearly revealed the existence of crystal plane fringes on each ZnO nanograin (NG) and Bi<sub>2</sub>O<sub>3</sub> and In<sub>2</sub>O<sub>3</sub> NIs. Further, to calculate the spacing between the planes of the crystals of n-ZnO/p-Bi<sub>2</sub>O<sub>3</sub> and ZnO-In<sub>2</sub>O<sub>3</sub>, inverse FFT (IFFT) image processing was utilized as depicted in Fig. 2(b and e). Based on IFFT image analysis, the *d*-spacing value of ZnO NGs was calculated to be 2.48 Å, corresponding to the [101] plane, and 2.72 Å for Bi<sub>2</sub>O<sub>3</sub> NIs, associated with the [121] lattice for n-ZnO/p-Bi<sub>2</sub>O<sub>3</sub> HNFs.<sup>47</sup> In the case of ZnO/In<sub>2</sub>O<sub>3</sub> HNFs, the *d*-spacing of ZnO was estimated as 2.81 Å which revealed the [100] plane and *d*-spacing of 3.89 Å corresponding to In<sub>2</sub>O<sub>3</sub> NIs that can be correlated to the [012] plane.<sup>48</sup> The analogous SAED patterns of the HNFs clearly revealed the multi-crystalline nature of the materials with nanograined structure as shown in Fig. 2(c and e). Multi-crystalline, concentric diffraction rings appeared in SAED patterns illustrating ZnO (104), Bi<sub>2</sub>O<sub>3</sub> (223), Bi<sub>2</sub>O<sub>3</sub> (330), Bi<sub>2</sub>O<sub>3</sub> (221), ZnO (100), Bi<sub>2</sub>O<sub>3</sub> (031), ZnO (110), ZnO (200), ZnO (001) and ZnO (211) lattice planes (Fig. 2(c)) as referred to JCPDS card no. 36-1451 for wurtzite ZnO and correspondingly monoclinic α-Bi<sub>2</sub>O<sub>3</sub> referred to JCPDS card no. 71-0465 for n-ZnO/p-Bi<sub>2</sub>O<sub>3</sub> HNFs. Similarly, coaxial ring observed in the SAED pattern of n-ZnO/n-In<sub>2</sub>O<sub>3</sub> HNFs depicted in Fig. 2(f) specifies the nature of polycrystallinity in the NGs corresponding to wurtzite ZnO and rhombohedral In<sub>2</sub>O<sub>3</sub>. The SAED pattern further revealed the features of ZnO (203), ZnO (104), ZnO (112), In<sub>2</sub>O<sub>3</sub> (116), In<sub>2</sub>O<sub>3</sub> (202), ZnO (101), In<sub>2</sub>O<sub>3</sub> (012), ZnO (100), ZnO (002), In<sub>2</sub>O<sub>3</sub> (024), In<sub>2</sub>O<sub>3</sub> (300), ZnO (104) and In<sub>2</sub>O<sub>3</sub> (128) lattice planes which were matched with standard for In<sub>2</sub>O<sub>3</sub> (JCPDS card no. 73-1809).<sup>47,49</sup> The HNFs exhibited nanograined morphology due to their intrinsic porosity and abundant surface area formed during the calcination process which could emboss n-ZnO/p-Bi<sub>2</sub>O<sub>3</sub> and n-ZnO/n-In<sub>2</sub>O<sub>3</sub> HNFs as efficient sensing materials with reduced operating temperature. The results indicated the existence of heterojunctions in the ZnO/Bi<sub>2</sub>O<sub>3</sub> and ZnO/In<sub>2</sub>O<sub>3</sub> HNFs at the interfaces. However, n-ZnO/p-Bi<sub>2</sub>O<sub>3</sub> and ZnO/In<sub>2</sub>O<sub>3</sub> HNFs showed typical nanograined structure with randomly oriented secondary p- and n-type MOS NIs. Possible alignment of the Fermi level with these secondary MOS nanograins occurs which could increase the overall electron density in both the HNF materials. Therefore, a corresponding increase in the rate of adsorption of NO<sub>2</sub> through electronic sensitization could be possibly expected.

The porous structure of ZnO/Bi<sub>2</sub>O<sub>3</sub> and ZnO/In<sub>2</sub>O<sub>3</sub> HNFs was revealed from TEM analysis, which was further quantified

using BET analysis. Detailed N<sub>2</sub> adsorption-desorption analyses of pristine ZnO, n-ZnO/p-Bi<sub>2</sub>O<sub>3</sub> and n-ZnO/n-In<sub>2</sub>O<sub>3</sub> HNFs are shown in Fig. S3 (ESI<sup>†</sup>). BET surface area, pore volume and pore size for these HNFs were estimated from the BJH plots as summarized in Table S1 (ESI<sup>†</sup>). The specific surface area was estimated to be 16.012 m<sup>2</sup> g<sup>-1</sup> and 7.302 m<sup>2</sup> g<sup>-1</sup> and the corresponding pore volume was 3.52 cm<sup>3</sup> g<sup>-1</sup> and 2.84 cm<sup>3</sup> g<sup>-1</sup> for n-ZnO/p-Bi<sub>2</sub>O<sub>3</sub> and n-ZnO/n-In<sub>2</sub>O<sub>3</sub> HNFs, respectively. The enhanced surface area of HNFs results in abundant surface-active sites compared with bare ZnO NFs which provided facile electron transport and thereby enhanced the rate of NO<sub>2</sub> adsorption.<sup>50</sup>

### 3.3. XPS analysis of ZnO/Bi<sub>2</sub>O<sub>3</sub> and ZnO/In<sub>2</sub>O<sub>3</sub> HNFs

In order to examine the interactions among n- and p-type MOS and n- and n-type MOS in the ZnO/Bi<sub>2</sub>O<sub>3</sub> and ZnO/In<sub>2</sub>O<sub>3</sub> HNFs and oxidation states of the elements, surface-sensitive X-ray photoelectron spectroscopic analysis was performed for pristine ZnO, n-ZnO/p-Bi<sub>2</sub>O<sub>3</sub> and n-ZnO/n-In<sub>2</sub>O<sub>3</sub> HNFs. Fig. 3(a) depicts the wide scan survey of pure ZnO, n-ZnO/p-Bi<sub>2</sub>O<sub>3</sub> and n-ZnO/n-In<sub>2</sub>O<sub>3</sub> HNFs, which revealed the presence of elemental peaks such as those of Zn, Bi, In and O which further confirms the absence of impurities in the HNFs. Fig. 3(b) displays the high-resolution Zn 2p XPS peaks corresponding to pristine ZnO, n-ZnO/p-Bi<sub>2</sub>O<sub>3</sub> and n-ZnO/n-In<sub>2</sub>O<sub>3</sub> HNFs. Fine scan of the Zn 2p peak reveals the incidence of two major peaks at binding energy of 1021.43 eV and 1044.68 eV attributed to Zn 2p<sub>3/2</sub> and Zn 2p<sub>1/2</sub> correspondingly, with an energy difference of 23.25 eV which indicated the bivalent oxidation state of ZnO NFs. Whereas, n-ZnO/p-Bi<sub>2</sub>O<sub>3</sub> and n-ZnO/n-In<sub>2</sub>O<sub>3</sub> HNFs revealed a minor shift to lower binding energy compared to pristine ZnO NFs owing to the surface lodging of Bi<sub>2</sub>O<sub>3</sub> and In<sub>2</sub>O<sub>3</sub> NIs and the presence of Zn<sub>i</sub> defects in the NG morphology.

The high-resolution spectra of the O 1s band of n-ZnO/p-Bi<sub>2</sub>O<sub>3</sub> and n-ZnO/n-In<sub>2</sub>O<sub>3</sub> HNFs are shown in Fig. 3(c). The O 1s peaks in pure ZnO, n-ZnO/p-Bi<sub>2</sub>O<sub>3</sub> and n-ZnO/n-In<sub>2</sub>O<sub>3</sub> HNFs were deconvoluted into a couple of peaks indicating O<sub>I</sub> and O<sub>II</sub>; the one at 529.5 eV is attributed to lattice oxygen in Zn-O bonding and the other at 531.3 eV is associated with surface chemisorbed oxide species, either O<sup>-</sup> or O<sup>2-</sup> ions. It is noticed that the chemisorbed oxygen species is dominant in pure ZnO NFs as displayed in Fig. 3(c). However, O<sub>II</sub> peak was slightly suppressed in the cases of ZnO/In<sub>2</sub>O<sub>3</sub> and ZnO/Bi<sub>2</sub>O<sub>3</sub> nanofibers compared to O<sub>I</sub> peak owing to the formation of heterojunctions on ZnO nanofibers which could be correlated with the NO<sub>2</sub> sensing properties.<sup>42</sup> The intensity of O<sub>II</sub> peak was observed to be lower for n-ZnO/n-In<sub>2</sub>O<sub>3</sub> than for n-ZnO/p-Bi<sub>2</sub>O<sub>3</sub> HNFs due to fewer adsorbed surface oxide molecules. A corresponding shift in O 1s spectra also was observed at lower energy in contrast to bare ZnO NFs, which further confirmed the strong interaction at the ZnO/Bi<sub>2</sub>O<sub>3</sub> and ZnO/In<sub>2</sub>O<sub>3</sub> hetero-interfaces. Also, the existence of more active sites and catalytic behavior of Bi<sub>2</sub>O<sub>3</sub> and In<sub>2</sub>O<sub>3</sub> NGs at the interface can indicate these materials as active sensing materials.

Moreover, Fig. 3(d and e) shows the high-resolution peaks of Bi 4f and In 3d peaks for n-ZnO/p-Bi<sub>2</sub>O<sub>3</sub> and n-ZnO/n-In<sub>2</sub>O<sub>3</sub>



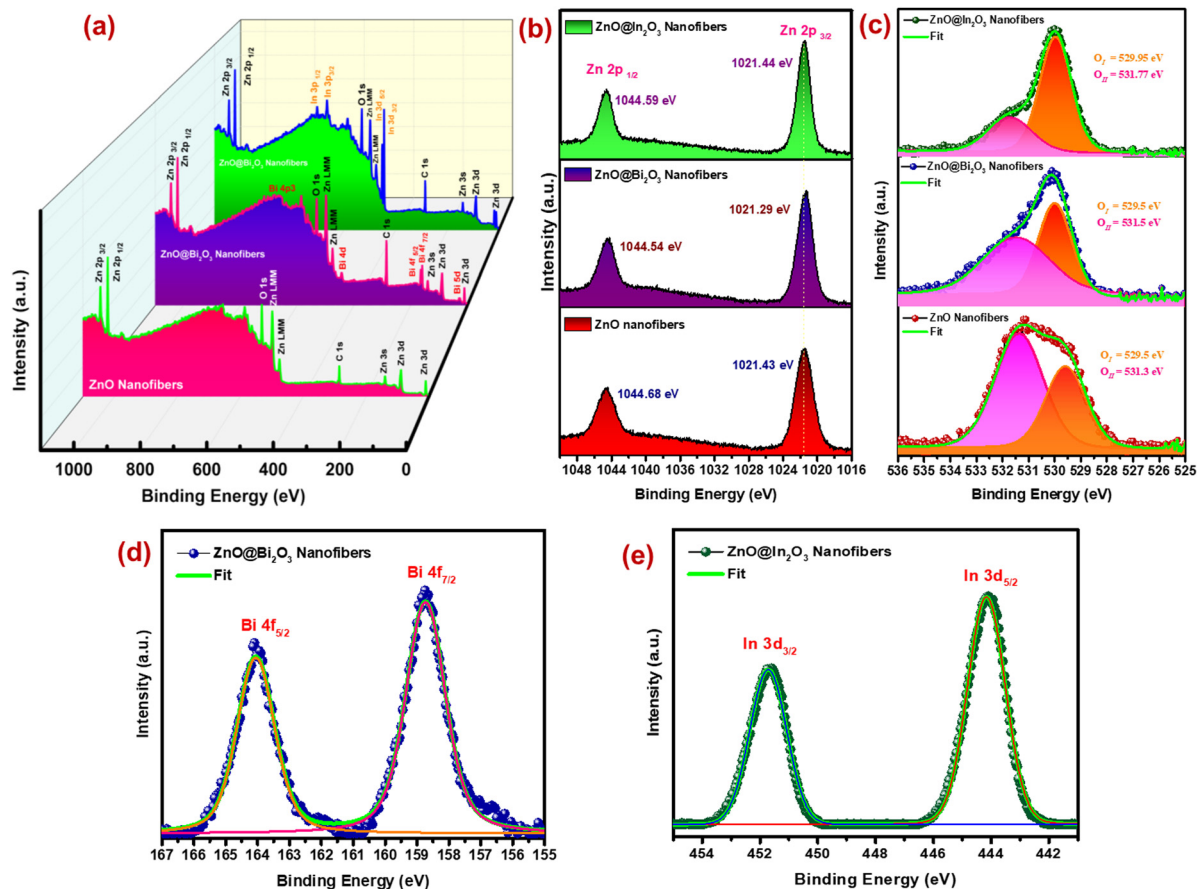


Fig. 3 (a) XPS wide scan spectra of bare ZnO, n-ZnO/p-Bi<sub>2</sub>O<sub>3</sub> and n-ZnO/n-In<sub>2</sub>O<sub>3</sub> HNFs. Fine scan spectra of (b) Zn 2p, (c) O 1s and (d) Bi 4f peaks of n-ZnO/p-Bi<sub>2</sub>O<sub>3</sub> and (e) In 3d peaks of n-ZnO/n-In<sub>2</sub>O<sub>3</sub> HNFs.

nanofibers, respectively. In the case of Bi<sub>2</sub>O<sub>3</sub>, the two peaks positioned at 158.7 and 163.8 eV are ascribed to Bi 4f<sub>7/2</sub> and Bi 4f<sub>5/2</sub> states as depicted in Fig. 3(d).<sup>51</sup> While, Fig. 3(e) presents the fine scan spectrum of In 3d state of n-ZnO/n-In<sub>2</sub>O<sub>3</sub> HNFs. For In<sub>2</sub>O<sub>3</sub>, the two peaks positioned at 442.8 and 450.4 eV are ascribed to In 3d<sub>5/2</sub> and In 3d<sub>3/2</sub> states, respectively.<sup>52</sup> The analysis of surface oxidation states of p-type Bi<sub>2</sub>O<sub>3</sub> and n-type In<sub>2</sub>O<sub>3</sub> NIs grown on the surface of ZnO nanofibers further confirmed the existence of heterointerfaces which is essential for enhanced sensor performance.

### 3.4. Evaluation of NO<sub>2</sub> sensing properties of aligned n-p type ZnO/Bi<sub>2</sub>O<sub>3</sub> and n-n type ZnO/In<sub>2</sub>O<sub>3</sub> HNFs

The aligned n-ZnO/p-Bi<sub>2</sub>O<sub>3</sub> and n-ZnO/n-In<sub>2</sub>O<sub>3</sub> HNFs were directly spun onto IDA transducer electrodes *via* the coaxial electrospinning method. Evaluation of NO<sub>2</sub> sensing properties of these sensor devices was performed using an in-house gas sensor test station existing in our laboratory.<sup>40</sup> Operating temperature of the HNFs has a vital role in enhancement in sensitivity and reliability of the sensor. The sensor response ( $S = [R_g - R_a]/R_a$ ) was monitored while purging of 1 ppm NO<sub>2</sub> gas with varying temperatures between 50 and 350 °C for pristine ZnO, n-ZnO/p-Bi<sub>2</sub>O<sub>3</sub> and n-ZnO/n-In<sub>2</sub>O<sub>3</sub> HNFs to determine the suitable operating temperature as shown in the insets

of Fig. 4(a and c). It was found that the maximum sensitivity ( $S$ ) toward 1 ppm of NO<sub>2</sub> gas was achieved at 300 °C and 200 °C for aligned n-ZnO/p-Bi<sub>2</sub>O<sub>3</sub> HNFs (324%) and aligned n-ZnO/n-In<sub>2</sub>O<sub>3</sub> HNFs (415%), respectively. The exposure time was fixed as 30 s for all measurements. The optimum temperature for which the maximum response occurred was further chosen as the working temperatures of the sensors. The highest sensitivity for the pristine ZnO nanofibers was attained at 250 °C. The operating temperature was reduced for aligned n-ZnO/n-In<sub>2</sub>O<sub>3</sub> HNFs compared with pristine ZnO, while that of aligned n-ZnO/p-Bi<sub>2</sub>O<sub>3</sub> nanofibers remained the same, but with superior sensitivity. This study clearly revealed the impact of n-n type heterojunctions with improved electron carrier density that favored enhanced NO<sub>2</sub> sensitivity. Even though the n-ZnO/p-Bi<sub>2</sub>O<sub>3</sub> nanofibers possess superior sensitivity, holes are the majority carriers for p-type Bi<sub>2</sub>O<sub>3</sub> semiconductor heterojunctions on ZnO nanofibers. The electron transfer among p-Bi<sub>2</sub>O<sub>3</sub> and n-ZnO arises owing to the work function difference which further leads to the occurrence of electron depletion at the interface. Therefore, the activation energy essential to achieve high sensitivity is significantly high due to charge transfer to p-Bi<sub>2</sub>O<sub>3</sub> nanoislands. However, the operating temperature of n-ZnO/p-Bi<sub>2</sub>O<sub>3</sub> nanofibers was not found to be excessive compared to pristine ZnO.



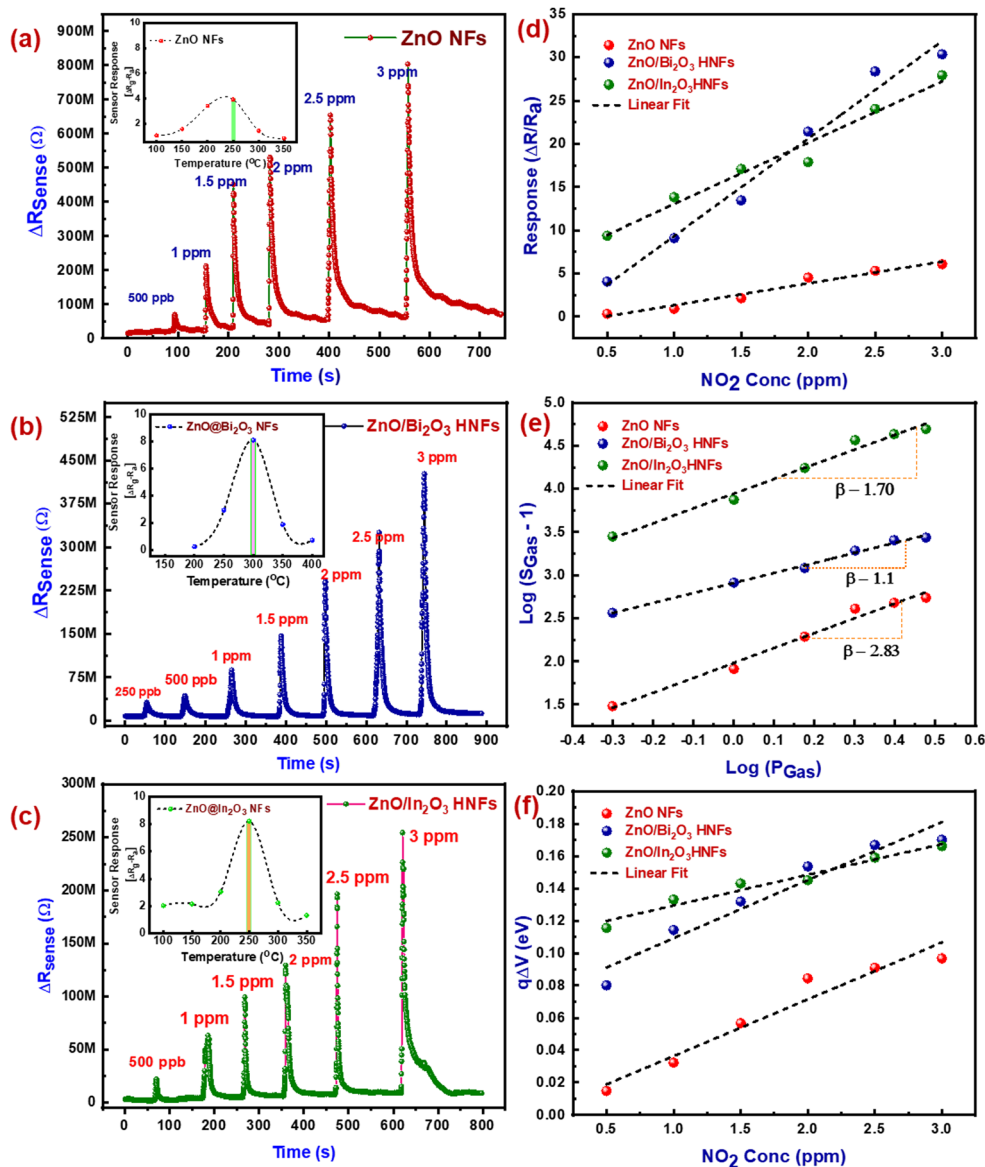


Fig. 4 Dynamic sensor response and recovery profiles of (a) porous ZnO NFs, (b) n-ZnO/p-Bi<sub>2</sub>O<sub>3</sub> HNFs and (c) n-ZnO/n-In<sub>2</sub>O<sub>3</sub> HNFs. (Insets show sensor response towards 1 ppm of NO<sub>2</sub> gas with varying temperature.) (d) Sensor response as a function of NO<sub>2</sub> concentration. (e) log(S<sub>Gas</sub> - 1) versus log(P<sub>Gas</sub>) plot. (f) Changes in band bending ( $q\Delta V$ ) with increase in NO<sub>2</sub> concentration.

The transient NO<sub>2</sub> responses of pristine ZnO, n-ZnO/p-Bi<sub>2</sub>O<sub>3</sub> and n-ZnO/n-In<sub>2</sub>O<sub>3</sub> based aligned HNFs for a concentration of NO<sub>2</sub> ranging from 500 ppb to 3 ppm are shown in Fig. 4(a–c). The variation in the resistance upon exposure to NO<sub>2</sub> gas indicates the surface reaction with the chemisorbed oxygen on the nanograined surface. The difference in resistance was observed to be enlarged with an increase in NO<sub>2</sub> concentration. The sensitivity ( $(R_g - R_a/R_a) \times 100\%$ ) as a function of concentration of NO<sub>2</sub> is depicted in Fig. 4(d). The results suggest a linear trend in the sensor response with increase in NO<sub>2</sub> concentration. The NO<sub>2</sub> gas sensing characteristics of the materials are tabulated in Table S2 (ESI<sup>†</sup>). The time required to attain 90% of variation in the overall resistance during/after exposure to NO<sub>2</sub> was used to calculate the sensor response and

recovery time. The NO<sub>2</sub> sensing characteristics shown in Table S2 (ESI<sup>†</sup>) indicate that the sensitivity of pristine ZnO nanofibers is up to 31% for 500 ppb concentration of NO<sub>2</sub> with response time of 9–10 s. Whereas, the n-ZnO/n-In<sub>2</sub>O<sub>3</sub> HNFs shows enhanced sensitivity of  $\sim 340\%$  with rapid response ( $t_{res(90)}$ ) of 4–5 s compared to n-ZnO/p-Bi<sub>2</sub>O<sub>3</sub> HNFs which exhibited a sensitivity of  $\sim 365\%$  with response time ( $t_{resp(90)}$ ) of 7–8 s. The boosted sensitivity observed for the HNFs was due to enhanced free carrier density at the heterojunction surface leading to fast charge transport while forming n–p and n–n heterojunctions. Prominently, the n-ZnO/n-In<sub>2</sub>O<sub>3</sub> HNFs operated at reduced temperature with superior sensitivity owing to the charge transfer from n-In<sub>2</sub>O<sub>3</sub> to n-ZnO owing to the work function variance. Therefore, charge accumulation could take





place on ZnO, while charge depletion occurs at the In<sub>2</sub>O<sub>3</sub> interfaces.

In order to investigate the chemisorbed oxygen species formed over the aligned ZnO/Bi<sub>2</sub>O<sub>3</sub> and ZnO/In<sub>2</sub>O<sub>3</sub> based HNFs, the slope of  $\log(S_{\text{Gas}} - 1)$  versus  $\log(P_{\text{Gas}})$  was estimated as shown in Fig. 4(e). Moreover, from the relation ( $S = aC^\beta$ ), the value of the exponent  $\beta$  could be used to understand the elementary reaction occurring on the material surface.<sup>53</sup> From the slope in Fig. 4(e), the  $\beta$  values were estimated as 0.56 for aligned n-ZnO/n-In<sub>2</sub>O<sub>3</sub> HNFs and 1.06 for aligned n-ZnO/p-Bi<sub>2</sub>O<sub>3</sub> HNFs at the operational temperature signifying that the surface adsorbed oxygen ions majorly could be O<sup>-</sup> rather than O<sup>2-</sup> ions. It was established by previous reports that if  $\beta$  is near to  $\sim 0.5$ , O<sup>2-</sup> ions could be adsorbed predominantly, and if  $\beta$  is  $\sim 1$ , surface oxide ion species are mostly O<sup>-</sup>.<sup>54</sup>

Aligned HNFs have shown improved sensitivity due to the presence of more energetic O<sup>-</sup> ions which are chemically more active compared to O<sub>2</sub><sup>-</sup> and could create additional favorable sites for surface catalytic processes. Upon exposure to NO<sub>2</sub>, the work function, electron affinity and surface band bending ( $q\Delta V$ ) of the sensing materials tend to change. The surface band bending energies of both aligned ZnO/Bi<sub>2</sub>O<sub>3</sub>- and ZnO/In<sub>2</sub>O<sub>3</sub>-based HNFs were estimated based on their sensor responses. The band bending values ( $q\Delta V$ ) were estimated for these HNFs based on their sensor response to varied NO<sub>2</sub> concentrations.<sup>55,56</sup> On analyzing  $q\Delta V$  of the HNFs, it was found that n-ZnO/n-In<sub>2</sub>O<sub>3</sub> HNFs possessed higher energy than n-ZnO/p-Bi<sub>2</sub>O<sub>3</sub> HNFs and pure n-ZnO NFs, because of a broad depletion region while purging NO<sub>2</sub> as evident from Fig. 4(f).

Selectivity towards NO<sub>2</sub> for n-ZnO/p-Bi<sub>2</sub>O<sub>3</sub> and n-ZnO/n-In<sub>2</sub>O<sub>3</sub> HNFs was further studied in the presence of possible interfering vapors such as NH<sub>3</sub>, H<sub>2</sub>S, SO<sub>2</sub>, C<sub>2</sub>H<sub>5</sub>OH and C<sub>3</sub>H<sub>6</sub>O. Both 1D aligned n-ZnO/p-Bi<sub>2</sub>O<sub>3</sub> and n-ZnO/n-In<sub>2</sub>O<sub>3</sub> HNFs revealed excellent selectivity towards NO<sub>2</sub> at operating temperature due to the favored electron transport characteristics as a result of the existence of surface-anchored p-Bi<sub>2</sub>O<sub>3</sub>/n-In<sub>2</sub>O<sub>3</sub> nanoclusters and intrinsic surface defect-mediated sensing properties as described in Fig. S4 (ESI<sup>†</sup>). Further, intervention of atmospheric moisture in the RH range of 10–95% on aligned n-ZnO/p-Bi<sub>2</sub>O<sub>3</sub> and n-ZnO/n-In<sub>2</sub>O<sub>3</sub> HNFs during NO<sub>2</sub> sensing was examined as shown in Fig. S5(a and b) (ESI<sup>†</sup>). When the relative humidity was increased, the sensor response was found to be deteriorated for aligned n-ZnO/p-Bi<sub>2</sub>O<sub>3</sub> HNFs owing to the interruption of hydroxide molecules which prevail on the HNF surface, reducing the flow of electrons. Whereas, aligned n-ZnO/n-In<sub>2</sub>O<sub>3</sub> HNFs show a slight decrease in sensitivity as revealed from Fig. S5(b) (ESI<sup>†</sup>) and a relatively even response over the relative humidity range of 10–40%, owing to the higher charge carrier density along with abundant surface-active sites. When the humidity content increased above 40%, the interruption of moisture was found to be persistent on the HNFs which decreases the charge transport and thereby decreases the rate of adsorption of NO<sub>2</sub> molecules. Furthermore, the response-recovery properties of aligned ZnO/Bi<sub>2</sub>O<sub>3</sub> and ZnO/In<sub>2</sub>O<sub>3</sub> HNFs were determined before and after 8 months for trace-level (1 ppm) NO<sub>2</sub> under working conditions as shown in Fig. S6(a–d) (ESI<sup>†</sup>).

Both 1D aligned n-ZnO/p-Bi<sub>2</sub>O<sub>3</sub> and n-ZnO/n-In<sub>2</sub>O<sub>3</sub> HNFs exhibited considerable stability even after 8 months during multiple cycles of NO<sub>2</sub> exposure. Though a minimal 15% drop in the sensitivity was perceived, stable base resistance values were sustained under operational conditions, which proves the durability and repeatability of the HNF sensors.

### 3.5. *In situ* AC impedance studies of aligned n-ZnO/p-Bi<sub>2</sub>O<sub>3</sub> and n-ZnO/n-In<sub>2</sub>O<sub>3</sub> HNFs-based sensors

In order to explore the mechanism behind enhanced sensor performance associated with surface anchoring of p-Bi<sub>2</sub>O<sub>3</sub> and n-In<sub>2</sub>O<sub>3</sub> nanoclusters on nanograined n-ZnO nanofibers, *in situ* AC impedance spectroscopic studies were carried out in various atmospheric conditions such as room temperature condition, sensor operating temperature and while purging NO<sub>2</sub>. Impedance spectroscopic measurements were acquired using a solid-state two-electrode system. Scheme 2 shows a schematic representation of impedance analysis performed under various conditions. *In situ* Nyquist plots in the frequency range of 20 Hz to 10 MHz acquired for 1D aligned n-ZnO/p-Bi<sub>2</sub>O<sub>3</sub> and n-ZnO/n-In<sub>2</sub>O<sub>3</sub> are depicted in Fig. 5(a and b).

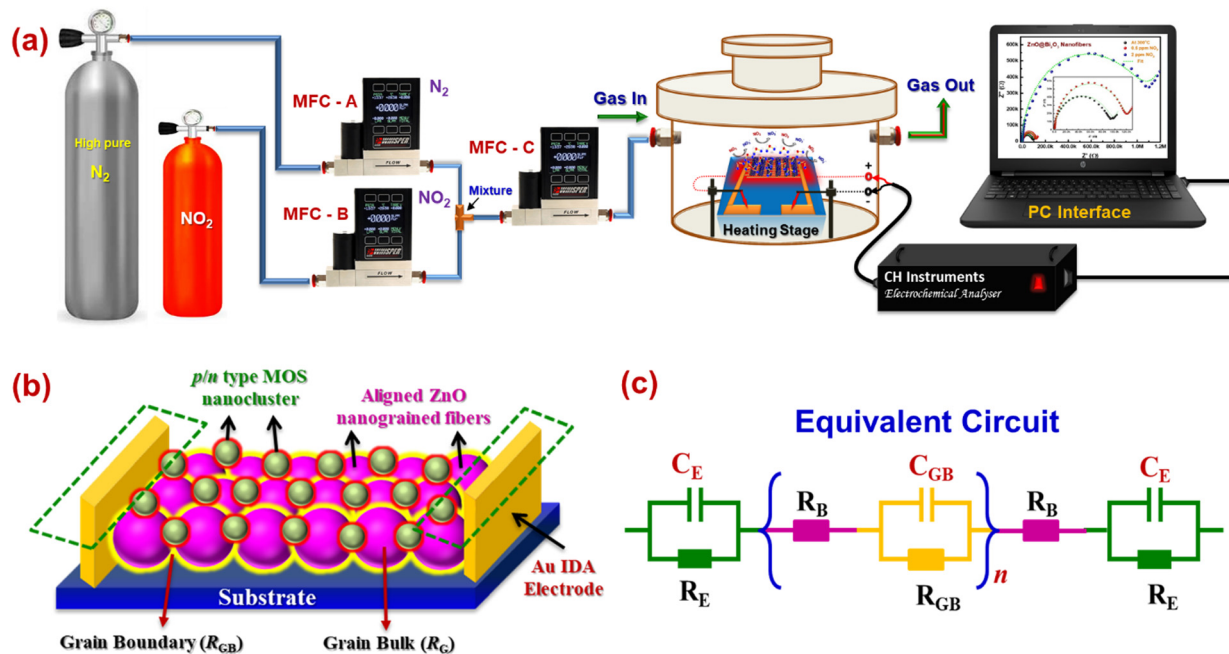
Prior to the *in situ* studies, Nyquist plots for ZnO/Bi<sub>2</sub>O<sub>3</sub> and ZnO/In<sub>2</sub>O<sub>3</sub> were acquired under ambient conditions and operating temperature to explore the charge transport phenomenon. At room temperature, both ZnO/Bi<sub>2</sub>O<sub>3</sub> and ZnO/In<sub>2</sub>O<sub>3</sub> HNFs possessed minimal conductivity as evident from the distorted *I*-*S* spectra as shown in Fig. S7(a and b) (ESI<sup>†</sup>). Whereas, as the conductivity of the sensor increased, the imaginary component ( $Z''$ ) versus the real component ( $Z'$ ) in the impedance spectra exhibited a perfect semicircle trend from low-frequency to high-frequency region, upon elevating the temperature up to operating temperature confirming the typical semiconductor behaviour.<sup>57</sup> Moreover, the characteristic semicircle arc followed by the Nyquist spectra confirms the grain–grain boundary induced conduction mechanism and the diameter of the semicircle was increased with respect to NO<sub>2</sub> concentration. The high-frequency region in the impedance spectra represents the material's grain-bulk ( $Z_G$ ) characteristics, median-frequency region signifies the grain boundary ( $Z_{GB}$ ) characteristics and lower-frequency region indicates the electrode to material contact characteristics.<sup>38</sup> The corresponding electrical equivalent circuit model was used to understand the major contribution either by nanograins or by grain boundaries, or the heterojunctions in the nanofibers.

The circuit model is expressed as a set of resistor–capacitor (RC) series circuit components as indicated in the insets of Fig. 5(a and b). The net impedance ( $Z_1$ ) of ZnO/Bi<sub>2</sub>O<sub>3</sub> and ZnO/In<sub>2</sub>O<sub>3</sub> HNFs is expressed as<sup>38</sup>

$$Z_1 = Z_0 + Z_G + Z_{GB} \quad (1)$$

where  $Z_0$  denotes the impedance influenced by electrode-to-material contact,  $Z_{GB}$  signifies the impedance influenced by grain boundaries and  $Z_G$  signifies the influence of complex impedance resulting from grain bulk. Using the typical equivalent circuit shown as an inset in Fig. 5(a and b), the impedance spectra were fitted using *Z* fit EC-Lab, V10.30 to extract the





Scheme 2 (a) Schematic illustration of the experimental setup used for AC impedance studies. (b) Porous layer of p/n MOS decorated ZnO nanofibers aligned between Au IDA electrodes. (c) Corresponding equivalent circuit.

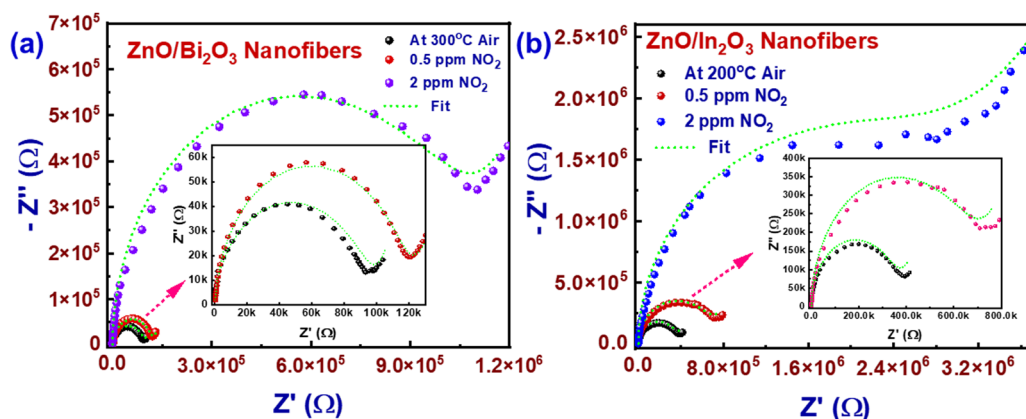


Fig. 5 *In situ* AC impedance measurements. Nyquist spectra of (a) ZnO/Bi<sub>2</sub>O<sub>3</sub> and (b) ZnO/In<sub>2</sub>O<sub>3</sub> HNFs at operating temperatures and during NO<sub>2</sub> exposure. Insets show the corresponding equivalent circuits.

parameters under operational conditions and under NO<sub>2</sub> atmosphere. Table S3 (ESI<sup>†</sup>) summarizes the estimated resistance components derived for ZnO/Bi<sub>2</sub>O<sub>3</sub> and ZnO/In<sub>2</sub>O<sub>3</sub> HNFs based sensors. The best fitted values with lower fitting errors were achieved as represented by dashed line, showing the best fitted parameters as listed in Table S3 (ESI<sup>†</sup>). The constant phase element (CPE) represented in the circuit model is to accommodate the non-ideal capacitor behaviour, due to inhomogeneous interface.

Nyquist plots for n-ZnO/p-Bi<sub>2</sub>O<sub>3</sub> and n-ZnO/n-In<sub>2</sub>O<sub>3</sub> HNFs were acquired under different temperatures and are depicted in Fig. S7(a and b) (ESI<sup>†</sup>). A reduced trend in the semicircle plot was observed which indicated that the resistance decreases as a function of temperature. This behaviour confirmed the

negative temperature coefficient of resistance (NTCR) owing to the semiconductor nature of the sensor materials used for this investigation. The results suggest that electrical conduction could be larger at high temperatures. In order to calculate the activation energy ( $E_a$ ), the following relation was used:<sup>53</sup>

$$R = R_0 \exp(-E_a/k_B T) \quad (2)$$

where  $R_0$  is pre-exponential factor,  $k_B$  is the Boltzmann constant and  $T$  is the temperature. The electrical conductivity values extracted from the complex impedance measurements for n-ZnO/p-Bi<sub>2</sub>O<sub>3</sub> and n-ZnO/n-In<sub>2</sub>O<sub>3</sub> HNFs demonstrate the semiconductor behaviour with an activation energy estimated to be  $E_a = 1.25$  eV and  $E_a = 1.15$  eV, respectively, as revealed in Fig. S7(c and d) (ESI<sup>†</sup>). Further, in order to estimate the optical



band gap of pure ZnO NFs, ZnO/Bi<sub>2</sub>O<sub>3</sub> and ZnO/In<sub>2</sub>O<sub>3</sub> HNFs, UV-DRS measurements were performed and the energy gaps were calculated using the Kubelka–Munk formulation as depicted in Fig. S2 (ESI†). It was observed that the band gap was decreased for ZnO/Bi<sub>2</sub>O<sub>3</sub> and ZnO/In<sub>2</sub>O<sub>3</sub> HNFs when compared to bare ZnO which confirms the favoured electronic coupling of HNFs.

The conduction mechanism of ZnO/Bi<sub>2</sub>O<sub>3</sub> and ZnO/In<sub>2</sub>O<sub>3</sub> HNFs-based sensors was further investigated during exposure to NO<sub>2</sub>. The impedance measurements were performed by purging of 100 sccm of 0.5–2 ppm concentration range of NO<sub>2</sub>. The acquired Nyquist spectra clearly show a decrease in the conductivity when the sensor was exposed to NO<sub>2</sub>. From the corresponding equivalent circuit, the resistances of grain and grain boundaries were estimated, which revealed the complex sensing phenomenon behind significant changes occurring upon NO<sub>2</sub> adsorption. Fig. 5(a and b) presents the Nyquist plots corresponding to n-ZnO/p-Bi<sub>2</sub>O<sub>3</sub> and n-ZnO/n-In<sub>2</sub>O<sub>3</sub> HNFs under air and NO<sub>2</sub> atmospheres. Nyquist spectra of both sensors under ambient environment showed negligible conductivity owing to the large Schottky barrier existing at the inter-grain interfaces. At working temperature in air condition of both n-ZnO/p-Bi<sub>2</sub>O<sub>3</sub> and n-ZnO/n-In<sub>2</sub>O<sub>3</sub> HNFs, grain bulk ( $Z_G$ ) and grain boundary ( $Z_{GB}$ ) resistances of HNFs have equal contributions towards charge transfer owing to the higher electron mobility. When exposed to 0.5 ppm NO<sub>2</sub>, the major contribution was found to be from nanofiber grain boundary rather than the contribution from the grain bulk for n-ZnO/p-Bi<sub>2</sub>O<sub>3</sub> and n-ZnO/n-In<sub>2</sub>O<sub>3</sub> HNFs as quantified in Table S3 (ESI†). It is evident that only the barrier potential of grain boundaries gets altered while grain bulk remains unchanged upon exposure to lower concentration since the NO<sub>2</sub> molecules trap free electrons from the surface of nanograins. Moreover, large change in the grain bulk and grain-boundary resistances was observed for n-ZnO/p-Bi<sub>2</sub>O<sub>3</sub> and n-ZnO/n-In<sub>2</sub>O<sub>3</sub> HNFs for 2 ppm of NO<sub>2</sub>, which may be the cause of the superior sensitivity compared to bare ZnO.

The barrier potential of grain bulk and grain boundary increases for both n-ZnO/p-Bi<sub>2</sub>O<sub>3</sub> and n-ZnO/n-In<sub>2</sub>O<sub>3</sub> HNFs owing to the strong interaction of NO<sub>2</sub> with the surface adsorbates (O<sup>-</sup> ions) and thereby pulling more electrons from the grain bulk ( $Z_G$ ). The results suggest that at the sensor operating temperature, more free electrons originate due to the charge transfer process occurring at the n–p and n–n interfaces of HNFs. When the sensors were exposed to trace-level concentration of NO<sub>2</sub>, these free electrons were trapped *via* surface adsorbed molecular oxygen (O<sup>-</sup>) and thereby captured more electrons from the interfacial grain boundaries of the HNFs. Upon exposure to higher concentration of NO<sub>2</sub>, along with grain boundaries ( $Z_{GB}$ ), NO<sub>2</sub> could abstract additional electrons from the grain bulk ( $Z_G$ ) thereby increasing the sensor resistance rapidly which increased the potential barrier height. This result further confirmed that the grain boundary ( $Z_{GB}$ ) of ZnO/Bi<sub>2</sub>O<sub>3</sub> and ZnO/In<sub>2</sub>O<sub>3</sub> HNFs is largely affected by NO<sub>2</sub> molecules which remained as the major reason behind the superior conduction in the HNFs.

The transport characteristics such as charge carrier density and width of the depletion layer were further estimated from the *in situ* impedance spectroscopic analysis under different conditions. Based on the Poisson equation, the relation between the barrier potential height and capacitance can be derived from the depletion approximation given as

$$C = \sqrt{\frac{e\epsilon_0\epsilon_r N_d}{2\phi}} \quad (3)$$

where  $C$  is the capacitance,  $e$  is the charge of electron,  $\epsilon_r$  and  $\epsilon_0$  are the permittivity of the materials and free space, respectively,  $N_d$  is the charge carrier density and  $\phi$  is the barrier height derived from the activation energy. Substituting the capacitance value calculated from the Nyquist plot fitting, the carrier density and width of the depletion layer were estimated by using eqn (4) and (5):

$$N_d = \frac{2\phi C^2}{e\epsilon_0\epsilon_r} \quad (4)$$

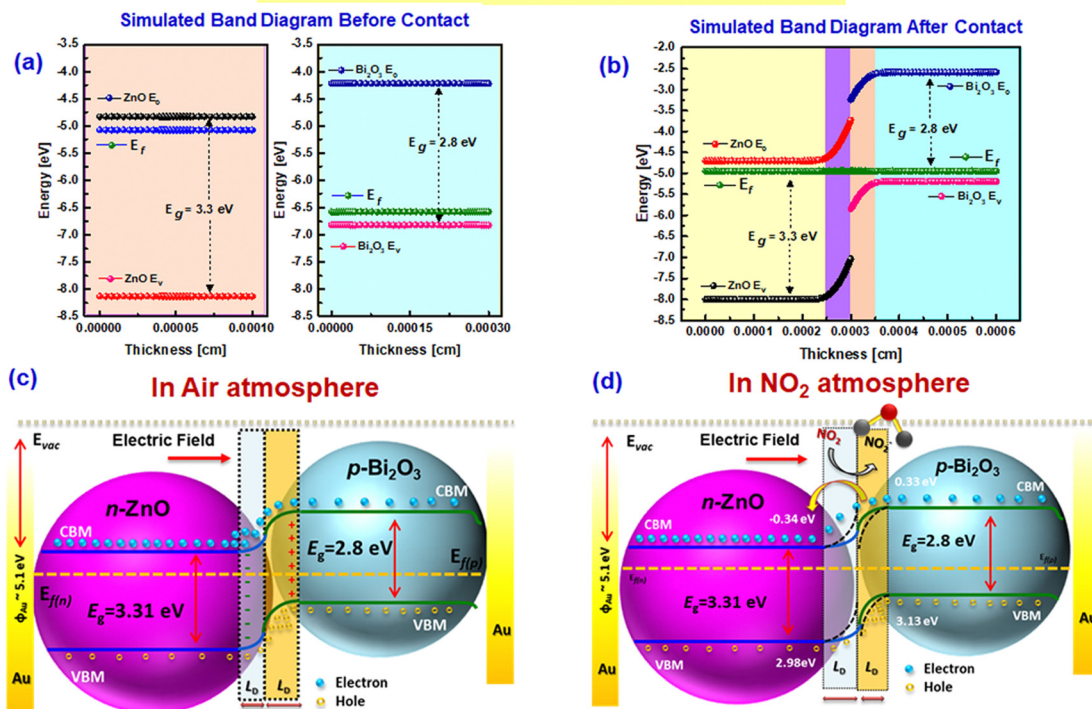
$$W = \left[ \frac{2\phi\epsilon_0\epsilon_r}{e^2 N_d} \right]^{1/2} \quad (5)$$

After introducing NO<sub>2</sub>, the carrier density ( $N_d$ ) was found to be reduced drastically from  $1.63 \times 10^{19}$  to  $0.98 \times 10^{19}$  cm<sup>-2</sup> for n-ZnO/p-Bi<sub>2</sub>O<sub>3</sub> and from  $1.44 \times 10^{19}$  to  $0.53 \times 10^{19}$  cm<sup>-2</sup> for n-ZnO/n-In<sub>2</sub>O<sub>3</sub> HNFs.<sup>58,59</sup>

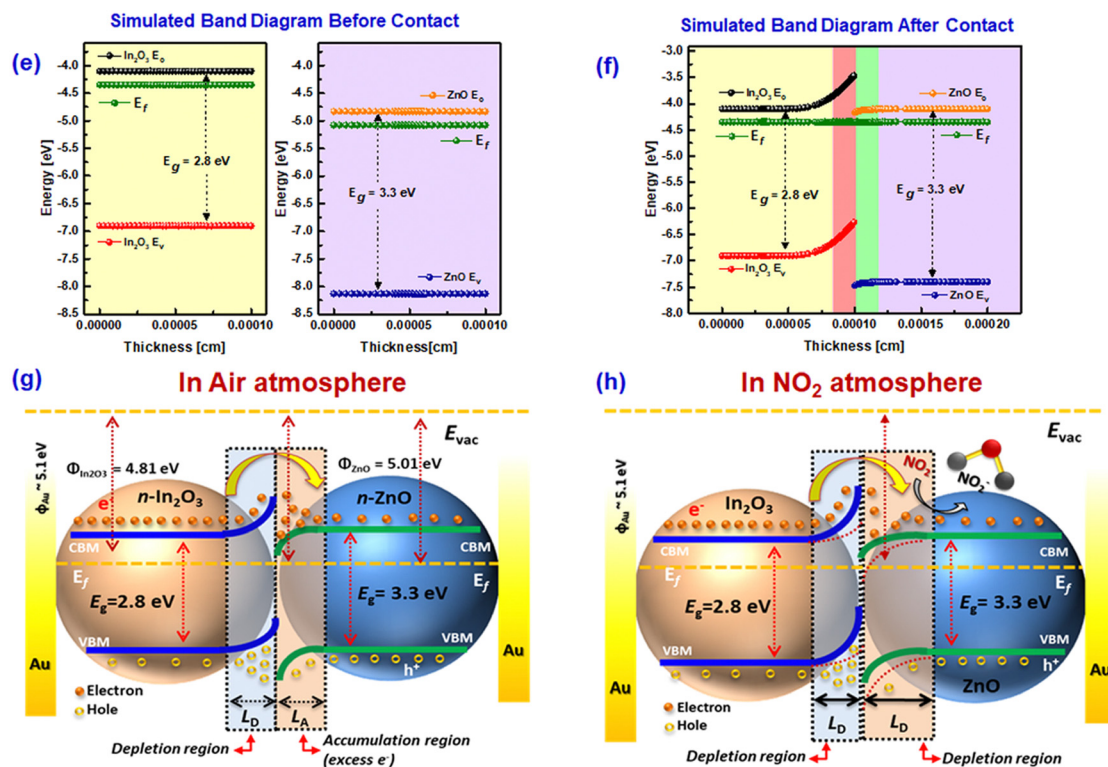
Accordingly, the depletion takes place on the surface of the HNFs due to reduction in the electron concentration as estimated by  $I$ – $S$  studies for n-ZnO/p-Bi<sub>2</sub>O<sub>3</sub> and n-ZnO/n-In<sub>2</sub>O<sub>3</sub> HNFs using eqn (5). The depletion layer width ( $W$ ) was observed to be enlarged from 2.16 nm to 2.76 nm for n-ZnO/p-Bi<sub>2</sub>O<sub>3</sub> and from 2.12 nm to 3.48 nm for n-ZnO/n-In<sub>2</sub>O<sub>3</sub> HNFs when NO<sub>2</sub> was purged at the working temperature and the results are summarized in Table S4 (ESI†). The reduction in charge carrier density is due to the charge recombination process during surface adsorption of NO<sub>2</sub> molecules on the HNFs which attract more electrons from the grain bulk and grain boundaries. Considering the aforementioned experimental results, it might therefore be confirmed that the difference in the rate of charge carrier density of n-ZnO/n-In<sub>2</sub>O<sub>3</sub> HNFs was found to be higher compared to n-ZnO/p-Bi<sub>2</sub>O<sub>3</sub> when exposed to NO<sub>2</sub>. However, from the AC impedance spectra, it was ascertained that the large variation of charge transport characteristics upon exposure to NO<sub>2</sub> is owing to the large accumulation of free charge carriers at the interface of n–n type ZnO/In<sub>2</sub>O<sub>3</sub> compared to that of n–p type heterojunction materials. Whereas, the built-in potential appearing while forming n–p type heterojunction slightly hinders the free charge carriers on the surface of the material owing to the presence of a hole accumulation regime. Under operational conditions, a large quantity of holes is accumulated by p-Bi<sub>2</sub>O<sub>3</sub> nanoclusters on the surface which leads to narrowing of the conduction channel of n-ZnO, and further thermal activation was required for greater response towards NO<sub>2</sub>. As observed from the AC impedance studies, the resistance of grain bulk and grain boundary nanojunction



### *n*-ZnO/*p*-Bi<sub>2</sub>O<sub>3</sub> Heterojunction Nanofibers



### *n*-ZnO/*n*-In<sub>2</sub>O<sub>3</sub> Heterojunction Nanofibers



**Scheme 3** (a, b, e and f) Simulated energy band diagram before and after contact. (c and d) Schematic representation of mechanism of band bending in *n*-ZnO/*p*-Bi<sub>2</sub>O<sub>3</sub> HNFs before and after NO<sub>2</sub> exposure. (g and h) Schematic representation of band bending mechanism in *n*-ZnO/*n*-In<sub>2</sub>O<sub>3</sub> HNFs before and after NO<sub>2</sub> exposure.



increases during NO<sub>2</sub> exposure for both n–p and n–n type HNF materials which can be further explored along with great variation in the conduction mechanism among the two different combinations.

Typically, when the HNF-based sensors are exposed to air environment in operational conditions, adsorption of oxide ions on the HNF surface occurs which further traps freely available electrons leading to the formation of an electron depletion region over the HNF surface. Moreover, from  $\beta$  values derived from the response graph, the adsorbed oxygen species on aligned ZnO/Bi<sub>2</sub>O<sub>3</sub> and ZnO/In<sub>2</sub>O<sub>3</sub> HNFs were found to be O<sup>−</sup> rather than O<sub>2</sub><sup>−</sup> ions. In order to understand the energy levels of ZnO/Bi<sub>2</sub>O<sub>3</sub> and ZnO/In<sub>2</sub>O<sub>3</sub> HNFs, a hypothetical band structure was constructed by AFORS-HET v2.5, as represented in Scheme 3. Energy level bending characteristics of ZnO/Bi<sub>2</sub>O<sub>3</sub> and ZnO/In<sub>2</sub>O<sub>3</sub> HNFs before and after NO<sub>2</sub> exposure were discussed in our previous report.<sup>54,60</sup> When n- and p-type MOS are electrically connected to form n–p heterojunctions, orientation of Fermi levels ( $E_f$ ) takes place as a result of work function difference; *i.e.*, electrons can move from higher occupied states to lower unoccupied states between the n-ZnO and p-Bi<sub>2</sub>O<sub>3</sub> heterojunctions further to align the  $E_f$  and thereby enhance the electron density.<sup>25,61</sup> Therefore, transferred electrons accumulate at the interface of the lower Fermi energy level and depletion takes place at the higher Fermi energy level junction which could continue until a stable equilibrium state is achieved. Whereas, feasible charge transport occurs near the interface of n–n junction (n-ZnO/n-In<sub>2</sub>O<sub>3</sub>) because of the minimal variances in the conduction band states. Consequently, an easy formation of electron accumulation at one junction is more dominant than forming a depletion region at the other interface. Hence, the conduction band with higher energy state (n-In<sub>2</sub>O<sub>3</sub>) exhibits a loss of electrons, whereas the conduction band with comparatively lower energy state (n-ZnO) receives more transferred electrons and forms an electron accumulation region. This results in subsequent ionosorption (O<sup>−</sup>) near the electron accumulation region and thereby widens the barrier potential and effectively increases the sensitivity towards NO<sub>2</sub> gas.<sup>62</sup> Hence, n-ZnO/n-In<sub>2</sub>O<sub>3</sub> HNFs exhibited enhanced sensitivity under reduced operating temperature.

Although the sensing mechanism was deduced in terms of energy band structure, the nature of sensing materials also plays a vital role in enhancing the rate of NO<sub>2</sub> adsorption. Though a 1D nanostructure offers better performance compared to other morphologies, the additional benefits from nanograined assisted 1D morphology leads to abundant active sites with high surface area and high aspect ratio. From the *in situ* impedance spectroscopic measurements, the conduction mechanism has been explored with the help of fitted equivalent circuits, which revealed the role of grains and grain boundary interactions in enhancing the NO<sub>2</sub> sensitivity. Hence, it is confirmed that the superior sensitivity is owing to the existence of ZnO/Bi<sub>2</sub>O<sub>3</sub> and ZnO/In<sub>2</sub>O<sub>3</sub> heterojunctions. The presence of ZnO nanograins with p-Bi<sub>2</sub>O<sub>3</sub> and n-In<sub>2</sub>O<sub>3</sub> formed in the multi-crystalline nanofibers induced abundant grain boundaries between these nanograins, which also act as a potential

barrier for further electron transfer. Upon exposure to NO<sub>2</sub>, the depletion region becomes wider and narrows the conduction channel due to expansion of depletion width. Therefore, the direct electron transport properties of multi-crystalline nanofibers make them promising as a better sensor material compared to crystalline nanorods. The results suggest that single-step production of MOS-based 1D aligned multi-crystalline HNFs could be a low-cost direct fabrication method for the development of superior real-time gas sensor devices with improved selectivity and likewise to bridge the gaps between the pilot-scale research and industrial manufacturing to make better products.

## 5. Conclusions

To summarize, aligned n-ZnO/p-Bi<sub>2</sub>O<sub>3</sub> and n-ZnO/n-In<sub>2</sub>O<sub>3</sub> HNFs produced using single-step on-chip fabrication have been demonstrated as active materials for NO<sub>2</sub> sensor application, the method using coaxial electrospinning which does not involve any tedious and time-consuming steps due to elimination of wet-chemical processes. Characterization of the materials affirmed the existence of heterojunctions in n-ZnO/p-Bi<sub>2</sub>O<sub>3</sub> and n-ZnO/n-In<sub>2</sub>O<sub>3</sub> HNFs and illustrated the presence of catalytic MOS nanoislands anchored uniformly on the surface of ZnO nanofibers. The operating temperature was increased for n-ZnO/p-Bi<sub>2</sub>O<sub>3</sub> (300 °C) and decreased for n-ZnO/n-In<sub>2</sub>O<sub>3</sub> HNFs (200 °C) compared to pristine ZnO NFs (250 °C). The improved sensitivity and selectivity of aligned n-ZnO/p-Bi<sub>2</sub>O<sub>3</sub> and n-ZnO/n-In<sub>2</sub>O<sub>3</sub> HNFs are attributed to the successful formation of n–p and n–n heterojunctions and more active sites, which resulted in fast response (5–7 s) and ten-fold higher response than ZnO nanofibers for trace-level concentration of NO<sub>2</sub> (500 ppb). It was confirmed that the enhanced NO<sub>2</sub> sensing properties are owing to the nature of nanograined NF structure along with sufficient active sites on the catalytic MOS nanoclusters, increasing the carrier density thereby trapping further O<sup>−</sup> ions on the HNF surface while creating more electron donors with higher barrier potential at the interfaces. The conduction mechanism based on electronic sensitization occurring in the HNFs was investigated using *in situ* AC impedance spectroscopic studies, which confirmed the role of modulation of grain bulk and grain boundary resistance and charge transfer between n–p and n–n type heterojunction materials. During *in situ* NO<sub>2</sub> exposure, the carrier density ( $N_d$ ) was found to be reduced drastically from  $1.63 \times 10^{19}$  to  $0.98 \times 10^{19}$  cm<sup>−2</sup> for n-ZnO/p-Bi<sub>2</sub>O<sub>3</sub> and from  $1.44 \times 10^{19}$  to  $0.53 \times 10^{19}$  cm<sup>−2</sup> for n-ZnO/n-In<sub>2</sub>O<sub>3</sub> HNFs. Accordingly, the depletion layer width ( $W$ ) was estimated which was found to be increased from 2.16 nm to 2.76 nm for n-ZnO/p-Bi<sub>2</sub>O<sub>3</sub> and from 2.12 nm to 3.48 nm for n-ZnO/n-In<sub>2</sub>O<sub>3</sub> HNFs. This investigation unveiled the complex sensing phenomenon related to electron transfer *via* grain–grain boundary interactions existing while forming a heterojunction with ZnO, which is the underlying major reason behind the enhancement of NO<sub>2</sub> sensing properties. Hence, 1D aligned MOS-based HNFs fabricated by a single-step process are promising for developing cost-effective NO<sub>2</sub> sensors with excellent sensitivity.



## Author contributions

Ramakrishnan Vishnuraj: methodology, conceptualization, NO<sub>2</sub> sensor analysis, *in situ* impedance spectroscopic analysis, data analysis, manuscript preparation. Mahaboobbatcha Aleem: energy band diagram simulation and analysis. Keerthi G Nair: XPS spectra fitting and analysis. Biji Pullithadathil: conceptualization, methodology, data analysis, manuscript preparation, supervision, resources and funding.

## Conflicts of interest

There are no conflicts to declare.

## Acknowledgements

The authors acknowledge Department of Science and Technology, Ministry of Science and Technology, India (ref. no. DST/TMD/HFC/2K18/55(C)) for financial support. The authors also wish to acknowledge the facilities and support provided by the management, PSG Sons and Charities, Coimbatore. The authors thank Dr Anuradha Ashok and Mr Vijayaraghavan, PSG IAS, Coimbatore for TEM measurements.

## References

- W. de Vries, Impacts of nitrogen emissions on ecosystems and human health: A mini review, *Curr. Opin. Environ. Sci. Health*, 2021, **21**, 100249.
- K. Sur, V. K. Verma and B. Pateriya, Variation of tropospheric NO<sub>2</sub> over Indo-Gangetic plain during COVID-19 outbreak in India, *Spat. Inf. Res.*, 2021, **29**, 841–855.
- H. Khan, A. Zavabeti, Y. Wang, C. J. Harrison, B. J. Carey, M. Mohiuddin, A. F. Chrimes, I. A. De Castro, B. Y. Zhang, Y. M. Sabri, S. K. Bhargava, J. Z. Ou, T. Daeneke, S. P. Russo, Y. Li and K. Kalantar-Zadeh, Quasi physisorptive two dimensional tungsten oxide nanosheets with extraordinary sensitivity and selectivity to NO<sub>2</sub>, *Nanoscale*, 2017, **9**, 19162–19175.
- W. Qin, Z. Yuan, H. Gao, R. Zhang and F. Meng, Perovskite-structured LaCoO<sub>3</sub> modified ZnO gas sensor and investigation on its gas sensing mechanism by first principle, *Sens. Actuators, B*, 2021, **341**, 130015.
- H. Zhu, Z. Yuan, Y. Shen, C. Han, H. Ji, Z. Mu and F. Meng, Conductometric acetic anhydride gas sensors based on S-doped porous ZnO microspheres with enhanced Lewis base interaction, *Sens. Actuators, B*, 2022, **373**, 132726.
- F. Meng, X. Shi, Z. Yuan, H. Ji, W. Qin, Y. B. Shen and C. Xing, Detection of four alcohol homologue gases by ZnO gas sensor in dynamic interval temperature modulation mode, *Sens. Actuators, B*, 2022, **350**, 130867.
- Y. Kang, F. Yu, L. Zhang, W. Wang, L. Chen and Y. Li, Review of ZnO-based nanomaterials in gas sensors, *Solid State Ionics*, 2021, **360**, 115544.
- J. Wang, M. Yu, X. Li and Y. Xia, UV-enhanced NO<sub>2</sub> gas sensing properties of polystyrene sulfonate functionalized ZnO nanowires at room temperature, *Inorg. Chem. Front.*, 2019, **6**, 176–183.
- A. Sharma, M. Tomar and V. Gupta, A low temperature operated NO<sub>2</sub> gas sensor based on TeO<sub>2</sub>/SnO<sub>2</sub> p-n hetero-interface, *Sens. Actuators, B*, 2013, **176**, 875–883.
- S. W. Choi, A. Katoch, J. H. Kim and S. S. Kim, Prominent reducing gas-sensing performances of n-SnO<sub>2</sub> nanowires by local creation of p-n heterojunctions by functionalization with p-Cr<sub>2</sub>O<sub>3</sub> nanoparticles, *ACS Appl. Mater. Interfaces*, 2014, **6**, 17723–17729.
- W. Maziarz, TiO<sub>2</sub>/SnO<sub>2</sub> and TiO<sub>2</sub>/CuO thin film nano-heterostructures as gas sensors, *Appl. Surf. Sci.*, 2019, **480**, 361–370.
- D. R. Miller, S. A. Akbar and P. A. Morris, Nanoscale metal oxide-based heterojunctions for gas sensing: A review, *Sens. Actuators, B*, 2014, **204**, 250–272.
- M. Nakamura, A. Sawa, J. Fujioka, M. Kawasaki and Y. Tokura, Interface band profiles of Mott-insulator/Nb: SrTiO<sub>3</sub> heterojunctions as investigated by optical spectroscopy, *Phys. Rev. B: Condens. Matter Mater. Phys.*, 2010, **82**, 4–7.
- F. Li, X. Gao, R. Wang, T. Zhang, G. Lu and N. Barsan, Design of Core-Shell Heterostructure Nanofibers with Different Work Function and Their Sensing Properties to Trimethylamine, *ACS Appl. Mater. Interfaces*, 2016, **8**, 19799–19806.
- Q. Sun, J. Wang, J. Hao, S. Zheng, P. Wan, T. Wang, H. Fang and Y. Wang, SnS<sub>2</sub>/SnS p-n heterojunctions with an accumulation layer for ultrasensitive room-temperature NO<sub>2</sub> detection, *Nanoscale*, 2019, **11**, 13741–13749.
- X. Zhang, Y. Liu, H. Liu, T. Liang, P. Zhang and Z. Dai, FeSe<sub>2</sub>/Hematite n-n heterojunction with oxygen spillover for highly efficient NO<sub>2</sub> gas sensing, *Sens. Actuators, B*, 2021, **345**, 130357.
- N. Kaur, M. Singh and E. Comini, One-Dimensional Nanostructured Oxide Chemoresistive Sensors, *Langmuir*, 2020, **36**, 6326–6344.
- S. Bai, H. Fu, Y. Zhao, K. Tian, R. Luo, D. Li and A. Chen, On the construction of hollow nanofibers of ZnO-SnO<sub>2</sub> heterojunctions to enhance the NO<sub>2</sub> sensing properties, *Sens. Actuators, B*, 2018, **266**, 692–702.
- H. Shin, W. G. Jung, D. H. Kim, J. S. Jang, Y. H. Kim, W. T. Koo, J. Bae, C. Park, S. H. Cho, B. J. Kim and I. D. Kim, Single-Atom Pt Stabilized on One-Dimensional Nanostructure Support via Carbon Nitride/SnO<sub>2</sub>Heterojunction Trapping, *ACS Nano*, 2020, **14**, 11394–11405.
- W. Avansi, A. C. Catto, L. F. Da Silva, T. Fiorido, S. Bernardini, V. R. Mastelaro, K. Aguir and R. Arenal, One-Dimensional V<sub>2</sub>O<sub>5</sub>/TiO<sub>2</sub> Heterostructures for Chemiresistive Ozone Sensors, *ACS Appl. Nano Mater.*, 2019, **2**, 4756–4764.
- S. Ng, J. Prášek, R. Zazpe, Z. Pytlíček, Z. Spötz, J. R. Pereira, J. Michalička, J. Příkryl, M. Krbal, H. Sopha, J. Hubálek and J. M. MacÁk, Atomic Layer Deposition of SnO<sub>2</sub>-Coated Anodic One-Dimensional TiO<sub>2</sub>Nanotube Layers for Low Concentration NO<sub>2</sub>Sensing, *ACS Appl. Mater. Interfaces*, 2020, **12**, 33386–33396.



- 22 V. Ramakrishnan, R. Unnathpadi and B. Pullithadathil, p-Co<sub>3</sub>O<sub>4</sub> supported heterojunction Carbon Nanofibers for Ammonia gas sensor applications, *J. Mater. Nanosci.*, 2022, **9**, 61–67.
- 23 T. Zhou and T. Zhang, Recent Progress of Nanostructured Sensing Materials from 0D to 3D: Overview of Structure–Property–Application Relationship for Gas Sensors, *Small Methods*, 2021, **5**, 1–32.
- 24 J. H. Kim, A. Katoch, S. H. Kim and S. S. Kim, Chemiresistive Sensing Behavior of SnO<sub>2</sub> (n)-Cu<sub>2</sub>O (p) Core-Shell Nanowires, *ACS Appl. Mater. Interfaces*, 2015, **7**, 15351–15358.
- 25 G. J. Sun, J. K. Lee, S. Choi, W. I. Lee, H. W. Kim and C. Lee, Selective Oxidizing Gas Sensing and Dominant Sensing Mechanism of n-CaO-Decorated n-ZnO Nanorod Sensors, *ACS Appl. Mater. Interfaces*, 2017, **9**, 9975–9985.
- 26 N. A. Isaac, I. Pikaar and G. Biskos, Metal oxide semiconducting nanomaterials for air quality gas sensors: operating principles, performance, and synthesis techniques, *Microchim. Acta*, 2022, **189**, 196, DOI: [10.1007/s00604-022-05254-0](https://doi.org/10.1007/s00604-022-05254-0).
- 27 M. Mousavi, M. B. Ghasemian, J. Han, Y. Wang, R. Abbasi, J. Yang, J. Tang, S. A. Idrus-Saidi, X. Guan, M. J. Christoe, S. Merhebi, C. Zhang, J. Tang, R. Jalili, T. Daeneke, T. Wu, K. Kalantar-Zadeh and M. Mayyas, Bismuth telluride topological insulator synthesized using liquid metal alloys: Test of NO<sub>2</sub> selective sensing, *Appl. Mater. Today*, 2021, **22**, 100954.
- 28 A. K. Elger and C. Hess, Application of Raman spectroscopy to working gas sensors: From in situ to operando studies, *Sensors*, 2019, **19**(23), 5075.
- 29 N. Sergent, M. Epifani, E. Comini, G. Faglia and T. Pagnier, Interactions of nanocrystalline tin oxide powder with NO<sub>2</sub>: A Raman spectroscopic study, *Sens. Actuators, B*, 2007, **126**, 1–5.
- 30 J. Zhang, D. Zeng, Q. Zhu, J. Wu, Q. Huang and C. Xie, Effect of Nickel Vacancies on the Room-Temperature NO<sub>2</sub> Sensing Properties of Mesoporous NiO Nanosheets, *J. Phys. Chem. C*, 2016, **120**, 3936–3945.
- 31 P. Hozák, M. Vorokhta, I. Khalakhan, K. Jarkovská, J. Cibulková, P. Fitl, J. Vlček, J. Fara, D. Tomeček, M. Novotný, M. Vorokhta, J. Lančok, I. Matolínová and M. Vršnata, New Insight into the Gas-Sensing Properties of CuOx Nanowires by Near-Ambient Pressure XPS, *J. Phys. Chem. C*, 2019, **123**, 29739–29749.
- 32 X. Xiao, L. Liu, J. Ma, Y. Ren, X. Cheng, Y. Zhu, D. Zhao, A. A. Elzatahry, A. Alghamdi and Y. Deng, Ordered Mesoporous Tin Oxide Semiconductors with Large Pores and Crystallized Walls for High-Performance Gas Sensing, *ACS Appl. Mater. Interfaces*, 2018, **10**, 1871–1880.
- 33 D. Degler, N. Barz, U. Dettinger, H. Peisert, T. Chassé, U. Weimar and N. Barsan, Extending the toolbox for gas sensor research: Operando UV/vis diffuse reflectance spectroscopy on SnO<sub>2</sub>-based gas sensors, *Sens. Actuators, B*, 2016, **224**, 256–259.
- 34 C. Drouilly, J. M. Krafft, F. Averseng, S. Casale, D. Bazer-Bachi, C. Chizallet, V. Lecocq, H. Vezin, H. Lauron-Pernot and G. Costentin, ZnO oxygen vacancies formation and filling followed by in situ photoluminescence and in situ EPR, *J. Phys. Chem. C*, 2012, **116**, 21297–21307.
- 35 S. C. Navale, V. Ravi, D. Srinivas, I. S. Mulla, S. W. Gosavi and S. K. Kulkarni, EPR and DRS evidence for NO<sub>2</sub> sensing in Al-doped ZnO, *Sens. Actuators, B*, 2008, **130**, 668–673.
- 36 F. Schipani, D. R. Miller, M. A. Ponce, C. M. Aldao, S. A. Akbar and P. A. Morris, Electrical Characterization of Semiconductor Oxide-Based Gas Sensors Using Impedance Spectroscopy: A Review, *Rev. Adv. Sci. Eng.*, 2016, **5**, 86–105.
- 37 H. S. Magar, R. Y. A. Hassan and A. Mulchandani, Electrochemical impedance spectroscopy (EIS): Principles, construction, and biosensing applications, *Sensors*, 2021, **21**(19), 6578, DOI: [10.3390/s21196578](https://doi.org/10.3390/s21196578).
- 38 V. Balasubramani, S. Sureshkumar, T. S. Rao and T. M. Sridhar, Impedance Spectroscopy-Based Reduced Graphene Oxide-Incorporated ZnO Composite Sensor for H<sub>2</sub>S Investigations, *ACS Omega*, 2019, **4**, 9976–9982.
- 39 Y. Wang, A. Maity, X. Sui, H. Pu, S. Mao, N. K. Singh and J. Chen, In Operando Impedance Spectroscopic Analysis on NiO-WO<sub>3</sub> Nanorod Heterojunction Random Networks for Room-Temperature H<sub>2</sub>S Detection, *ACS Omega*, 2018, **3**, 18685–18693.
- 40 R. Vishnuraj, J. Dhakshinamoorthy, K. G. Nair, M. Aleem and B. Pullithadathil, MEMS-compatible, gold nanoisland anchored 1D aligned ZnO heterojunction nanofibers: Unveiling the NO<sub>2</sub> sensing mechanism with: Operando photoluminescence studies, *Mater. Adv.*, 2021, **2**, 3000–3013.
- 41 D. V. Ponnuruvelu, S. Abdulla and B. Pullithadathil, Novel Electro-Spun Nanograined ZnO/Au Heterojunction Nanofibers and Their Ultrasensitive NO<sub>2</sub> Gas Sensing Properties, *ChemistrySelect*, 2018, **3**, 7156–7163.
- 42 S. Balachandran and M. Swaminathan, Facile fabrication of heterostructured Bi<sub>2</sub>O<sub>3</sub>-ZnO photocatalyst and its enhanced photocatalytic activity, *J. Phys. Chem. C*, 2012, **116**, 26306–26312.
- 43 F. Liu, G. Huang, X. Wang, X. Xie, G. Xu, G. Lu, X. He, J. Tian and H. Cui, High response and selectivity of single crystalline ZnO nanorods modified by In<sub>2</sub>O<sub>3</sub> nanoparticles for n-butanol gas sensing, *Sens. Actuators, B*, 2018, **277**, 144–151.
- 44 R. Zhang, P. G. Yin, N. Wang and L. Guo, Photoluminescence and Raman scattering of ZnO nanorods, *Solid State Sci.*, 2009, **11**, 865–869.
- 45 B. Karthikeyan, R. Udayabhaskar and A. Kishore, *Appl. Phys. A: Mater. Sci. Process.*, 2014, **117**, 1409–1414.
- 46 S. Sahoo, A. P. S. Gaur, A. K. Arora and R. S. Katiyar, Optical properties of In<sub>2</sub>O<sub>3</sub> octahedra nano-beads grown on ZnO nanowires, *Chem. Phys. Lett.*, 2011, **510**, 242–245.
- 47 Z. Xue, Z. Cheng, J. Xu, Q. Xiang, X. Wang and J. Xu, Controllable Evolution of Dual Defect ZnO and VO Associate-Rich ZnO Nanodishes with (0001) Exposed Facet and Its Multiple Sensitization Effect for Ethanol Detection, *ACS Appl. Mater. Interfaces*, 2017, **9**, 41559–41567.
- 48 Y. V. Kaneti, Z. Zhang, J. Yue, Q. M. D. Zakaria, C. Chen, X. Jiang and A. Yu, Crystal plane-dependent gas-sensing properties of zinc oxide nanostructures: Experimental and theoretical studies, *Phys. Chem. Chem. Phys.*, 2014, **16**, 11471–11480.



- 49 S. Bai, L. Quan, P. Tang, Y. Zhao, R. Luo, A. Chen, D. Li and N. Han, Controllable Synthesis and Gas-Sensing Properties of Zinc Oxide Nanocrystals with Exposed Different Percentage of Facets, *IEEE Sens. J.*, 2016, **16**, 866–872.
- 50 K. Zhang, S. Qin, P. Tang, Y. Feng and D. Li, Ultra-sensitive ethanol gas sensors based on nanosheet-assembled hierarchical ZnO-In<sub>2</sub>O<sub>3</sub> heterostructures, *J. Hazard. Mater.*, 2020, **391**, 122191.
- 51 J. Xu and J. Liu, Facet-selective epitaxial growth of  $\delta$ -Bi<sub>2</sub>O<sub>3</sub> on ZnO nanowires, *Chem. Mater.*, 2016, **28**, 8141–8148.
- 52 H. Liu, H. Zhai, C. Hu, J. Yang and Z. Liu, Hydrothermal synthesis of In<sub>2</sub>O<sub>3</sub> nanoparticles hybrid twins hexagonal disk ZnO heterostructures for enhanced photocatalytic activities and stability, *Nanoscale Res. Lett.*, 2017, **12**, 2–11.
- 53 J. Dhakshinamoorthy and B. Pullithadathil, New Insights Towards Electron Transport Mechanism of Highly Efficient p-Type CuO (111) Nanocuboids-Based H<sub>2</sub>S Gas Sensor, *J. Phys. Chem. C*, 2016, **120**, 4087–4096.
- 54 V. Ramakrishnan, K. G. Nair, J. Dhakshinamoorthy, K. R. Ravi and B. Pullithadathil, Porous, n-p type ultra-long, ZnO@Bi<sub>2</sub>O<sub>3</sub> heterojunction nanorods - Based NO<sub>2</sub> gas sensor: New insights towards charge transport characteristics, *Phys. Chem. Chem. Phys.*, 2020, **22**, 7524–7536.
- 55 M. E. Mazhar, G. Faglia, E. Comini, D. Zappa, C. Baratto and G. Sberveglieri, Kelvin probe as an effective tool to develop sensitive p-type CuO gas sensors, *Sens. Actuators, B*, 2016, **222**, 1257–1263.
- 56 M. Hübner, C. E. Simion, A. Tomescu-Stanoiu, S. Pokhrel, N. Bărsan and U. Weimar, Influence of humidity on CO sensing with p-type CuO thick film gas sensors, *Sens. Actuators, B*, 2011, **153**, 347–353.
- 57 A. Labidi, C. Jacolin, M. Bendahan, A. Abdelghani, J. Guérin, K. Aguir and M. Maaref, Impedance spectroscopy on WO<sub>3</sub> gas sensor, *Sens. Actuators, B*, 2005, **106**, 713–718.
- 58 K. Guruprasad, G. Marappan, S. Elangovan, S. Velappa Jayaraman, K. Kamala Bharathi, G. Venugopal, C. Di Natale and Y. Sivalingam, Electrical transport properties and impedance analysis of Au/ZnO nanorods/ITO heterojunction device, *Nano Express*, 2020, **1**, 030020, DOI: [10.1088/2632-959X/abc6f8](https://doi.org/10.1088/2632-959X/abc6f8).
- 59 F. Schipani, D. R. Miller, M. A. Ponce, C. M. Aldao, S. A. Akbar, P. A. Morris and J. C. Xu, Conduction mechanisms in SnO<sub>2</sub> single-nanowire gas sensors: An impedance spectroscopy study, *Sens. Actuators, B*, 2017, **241**, 99–108.
- 60 R. Vishnuraj, K. K. Karuppanan, M. Aleem and B. Pullithadathil, Boosting the performance of NO<sub>2</sub> gas sensors based on n-n type mesoporous ZnO@In<sub>2</sub>O<sub>3</sub> heterojunction nanowires: in situ conducting probe atomic force microscopic elucidation of room temperature local electron transport, *Nanoscale Adv.*, 2020, **2**, 4785–4797.
- 61 D. Zhang, Y. Cao, J. Wu and X. Zhang, Tungsten trioxide nanoparticles decorated tungsten disulfide nanoheterojunction for highly sensitive ethanol gas sensing application, *Appl. Surf. Sci.*, 2020, **503**, 144063.
- 62 K. V. Sopiha, O. I. Malyi, C. Persson and P. Wu, Chemistry of Oxygen Ion sorption on SnO<sub>2</sub> Surfaces, *ACS Appl. Mater. Interfaces*, 2021, **13**, 33664–33676.

